Inclusion of a dry surface layer and modifications to the transpiration and canopy evaporation partitioning in the Canadian Land Surface Scheme Including biogeochemical Cycles (CLASSIC)

Gesa Meyer[1], Joe R. Melton[2], and Elyn R. Humphreys[3]

[1]Environment and Climate Change Canada
[2]Environment Canada
[3]Carleton University

November 22, 2022

Abstract

Land surface/Earth System models depend upon accurate simulation of evapotranspiration (ET) to avoid excessive biases in simulated energy, water, and carbon cycles. The Canadian Land Surface Scheme including biogeochemical Cycles (CLASSIC), the land surface scheme of the Canadian Earth System Model (CanESM) shows reasonable ET fluxes globally, but CLASSIC's partitioning into evaporation (E) and transpiration (T) can be improved. Specifically, CLASSIC exhibited a high soil evaporation (Es) bias in sparsely vegetated areas during wet periods, which can deplete soil water and decrease photosynthesis and T later in the year.

A dry surface layer (DSL) parameterization was implemented to address biases in Es through an increased surface resistance to water vapour and heat fluxes. In arid/semi-arid regions, the DSL decreased Es, leading to improved seasonality of ET and increased gross primary productivity (GPP) due to an increase in soil moisture. The DSL simulations significantly (t-test, $p<0.01$) increased T/ET from 0.25 in baseline CLASSIC to 0.30 in the DSL simulations. T/ET was further increased to 0.41 ($p<0.01$), comparable to the CMIP5 model mean, by allowing T to occur from the dry canopy fraction while water evaporates from the wet fraction. This mainly affected densely vegetated areas, where T and ET increased significantly ($p<0.01$) and canopy E was reduced ($p<0.01$). In seasonally dry tropical forests, higher T and ET reduced GPP. Despite increases in arid/semi-arid regions, the reduced GPP in tropical forests resulted in 1.6% lower global GPP ($p=0.018$) than baseline CLASSIC. Including these modifications in CanESM might reduce biases in climate.

Inclusion of a dry surface layer and modifications to the transpiration and canopy evaporation partitioning in the Canadian Land Surface Scheme Including biogeochemical Cycles (CLASSIC)

Gesa Meyer[1], Joe R. Melton[1], Elyn R. Humphreys[2]

[1]Environment and Climate Change Canada, Climate Research Division, Victoria, BC, Canada
[2]Carleton University, Geography and Environmental Studies, Ottawa, ON, Canada

Key Points:

- Including a dry surface layer (DSL) parameterization reduced excessive soil evaporation (E_s) in CLASSIC globally, especially in dry regions
- Evapotranspiration (ET) partitioning modifications increased photosynthesis in arid/semi-arid regions
- Global transpiration (T) to ET ratios were brought closer to observation-based estimates due to increased T and reduced E_s in dry regions

Corresponding author: Gesa Meyer, gesa.meyer@ec.gc.ca

Abstract

Land surface/Earth System models depend upon accurate simulation of evapotranspiration (ET) to avoid excessive biases in simulated energy, water, and carbon cycles. The Canadian Land Surface Scheme including biogeochemical Cycles (CLASSIC), the land surface scheme of the Canadian Earth System Model (CanESM) shows reasonable ET fluxes globally, but CLASSIC's partitioning into evaporation (E) and transpiration (T) can be improved. Specifically, CLASSIC exhibited a high soil evaporation (E_s) bias in sparsely vegetated areas during wet periods, which can deplete soil water and decrease photosynthesis and T later in the year.

A dry surface layer (DSL) parameterization was implemented in CLASSIC to address biases in E_s through an increased surface resistance to water vapour and heat fluxes. In arid/semi-arid regions, the DSL decreased E_s, leading to improved seasonality of ET and increased gross primary productivity (GPP) due to an increase in soil moisture. The DSL simulations significantly (t-test, $p<0.01$) increased T/ET from 0.25 in baseline CLASSIC to 0.30 in the DSL simulations. T/ET was further increased to 0.41 ($p<0.01$), comparable to the CMIP5 model mean, by allowing T to occur from the dry canopy fraction while water evaporates from the wet fraction. This mainly affected densely vegetated areas, where T and ET increased significantly ($p<0.01$) and canopy E was reduced ($p<0.01$). In seasonally dry tropical forests, higher T and ET reduced soil moisture and GPP. Despite increases in arid/semi-arid regions, the reduced GPP in tropical forests resulted in ∼1.6% lower global GPP ($p=0.018$) than baseline CLASSIC. Including these modifications in CanESM might reduce biases in climate.

Plain Language Summary

An important component of the global water cycle is the return of liquid water to the atmosphere from the land surface. Evaporation (E) occurs on the surface of plants and the soil while transpiration (T) is water that plants release through their stomata. We investigated how well E and T are simulated by the Canadian Land Surface Scheme including biogeochemical Cycles (CLASSIC). We found that the model simulated the total amount of water lost from the land surface reasonably well, but too much was lost via E at the expense of T. To improve this we changed how water evaporates from bare soil to more realistically capture the resistance to evaporating water as a thin dry layer forms on the soil surface. We additionally allowed the model to transpire water from plant leaves while other leaves on the plant were wet and evaporating, which was previously not the case. Our results improve the partitioning of E and T in CLASSIC resulting in more realistic simulated plant productivity in dry regions.

1 Introduction

Evapotranspiration (ET) is an important component of the global terrestrial water budget, with about 60% of precipitation over land returned to the atmosphere via ET (Jung et al., 2010). ET can be separated into its components soil evaporation (E_s), canopy evaporation (E_c) and transpiration (T). These components draw water from different sources and their relative contributions to ET vary seasonally. While E_s mainly originates from the soil surface and shallow soil depths, T uses water accessible to plant roots and E_c occurs for a limited time following precipitation events, when water is on the vegetation canopy due to precipitation interception. E_s, E_c and T then also show different sensitivities to environmental drivers of ET such as vapor pressure deficit (VPD) and solar radiation (K. Wang & Dickinson, 2012). Total ET and the contributions of the different ET components vary significantly between ecosystems and seasons, as vegetation cover, vegetation characteristics, i.e. leaf area index (LAI) and rooting depths, and soil characteristics differ (K. Wang & Dickinson, 2012).

Available measurements of ET or latent (LE) and sensible heat fluxes (H) range temporally from half-hourly to annual and spatially from point-scale to hundreds of meters based upon techniques using lysimeters, eddy covariance or Bowen ratio methods and scintillometers (Barr et al., 1994; Baldocchi et al., 2001; Gavilán & Berengena, 2007; Malek & Bingham, 1993; Savage, 2009). On monthly to annual time scales over large regions, the surface water balance method can be used. It integrates measurements of precipitation, river discharges and estimates of changes in terrestrial water storage to determine LE on regional to global scales (L. Zhang et al., 2008; Güntner, 2008). Satellite remote sensing algorithms can estimate ET using empirical relationships with satellite-derived data (e.g., radiation, temperature, VPD) (Q. Mu et al., 2011). The relative contributions of the ET components can be estimated using several techniques. Canopy interception, which determines the amount of water available for E_c, can be estimated as the difference between total precipitation and the precipitation measured underneath the canopy (Herbst et al., 2008). For transpiration, sap flow methods can determine its value at the tree level, which can then be up-scaled to the stand or landscape level (Smith & Allen, 1996; Čermák et al., 2004; Warren et al., 2018). All three ET components, E_s, E_c and T, can also be measured with stable isotope techniques whereby variations in the stable isotopic composition of water vapour measured near the surface in combination with measurements of the isotopic composition of water from the soil and within the plant can determine the transpiration and evaporation fractions (Sutanto et al., 2014). However, direct measurements of ET and its components are only available at small scales (e.g., plant level), and thus there are large uncertainties in global T/ET with estimates varying between 0.43 and 0.75 with a mean value of 0.57 $\pm$ 0.07 (Wei et al., 2017). Most of global T originates from tropical forests (Good et al., 2015) with an estimated T/ET of 0.70 $\pm$ 0.14 (Schlesinger & Jasechko, 2014), while shrublands and desert ecosystems tend to have the lowest T/ET with estimated values of 0.47 $\pm$ 0.10 and 0.54 $\pm$ 0.18, respectively (Schlesinger & Jasechko, 2014).

Land surface models (LSMs) are used to simulate water and energy fluxes, including the different components of ET, for historical simulations and future projections. Despite challenges validating the different ET components on large scales, it is important for LSMs to correctly partition ET as it affects the water, energy and carbon (C) cycles (Swenson & Lawrence, 2014). Poorly simulated ET also has implications for the simulated climate in Earth System Models (ESMs). Dong et al. (2022) attributed a warm bias in 2 m air temperatures occurring in the central United States in models contributing to the Climate Model Intercomparison Project Phase 6 (CMIP6) to an underestimated ET and a low T/ET. In the CMIP6 models, ET is highly dependent on shallow soil moisture and water intercepted by the canopy while less dependent on root zone soil moisture. This leads to an underestimated contribution of T to ET, as well as a low total ET. Summertime ET in CMIP6 models was underestimated which was suggested to be a result of an overestimation of water stress, as the ESMs were not able to adequately simulate the ability of plants to access soil moisture in deeper layers, which can sustain T, and thereby were overly dependent on precipitation to supply near-surface soil moisture (Dong et al., 2022). While simulated ET partitioning varies between models, e.g. T/ET ranged from 0.20 to 0.57 (Lian et al., 2018), on average, the CMIP5 models underestimated T with an ensemble mean T/ET of 0.41 $\pm$ 0.11 (Lian et al., 2018) compared to the estimated 0.57 $\pm$ 0.07 (Wei et al., 2017) derived from upscaling site measurements using ecosystem-specific LAI regressions and LAI and canopy interception estimates from remote sensing and land surface models. As the underestimation of T/ET in ESMs leads to underestimations of summertime ET as well as overestimations of air temperature, improving ET partitioning in LSMs is important for future projections of the water and C cycles (Dong et al., 2022). Dong et al. (2020) suggest that E_s stress functions, commonly used in LSMs where they rely upon simple relationships with soil texture, cause biases in soil moisture-ET coupling in LSMs. Especially in bare soil areas or regions with sparse vegetation canopies, LSMs tend to overestimate ET due to an overestimation of E_s during periods of high soil moisture (Swenson & Lawrence, 2014). Over the past decade, studies have shown that simulated E_s can be improved by different means including resistance to E due to water vapour diffusion through a dry layer developing at the soil surface (Swenson & Lawrence, 2014), a viscous sublayer (Haghighi & Or, 2015; Decker et al., 2017) or a litter layer (Decker et al., 2017; M. Mu et al., 2021). Biases in simulated ET and its component fluxes were also shown to be reduced by an improved representation of the effects of soil texture in the E_s stress function, which decreased soil moisture-ET coupling strength biases in the Noah land surface model with multiparameterization options (Noah-MP version 3.6) (Dong et al., 2020).

In this study, we investigate ET and its component fluxes in the Canadian Land Surface Scheme Including biogeochemical Cycles (CLASSIC). In order to improve modelled E_s and T, a process-based ground evaporation efficiency parameterization, in which E_s is determined by water vapour diffusion through a thin dry surface layer (DSL) following Swenson and Lawrence (2014) was implemented. The partitioning into E_c and T was also modified such that the dry fraction of the canopy can transpire while E_c occurs from the wet canopy fraction following Fan et al. (2019). We compare the modified and baseline CLASSIC versions at the site-level as well as globally, evaluating them using eddy covariance or satellite-based observations of CO_2 and energy fluxes. Section 2 describes CLASSIC as well as the modifications made to its partitioning of ET. Section 3 shows the site-level and global water and carbon fluxes using the original CLASSIC, CLASSIC including the DSL parameterization and CLASSIC including the DSL as well as a modified partitioning into E_c and T. Differences between the carbon and water fluxes of the three CLASSIC versions, how they compare with other LSMs and possible future improvements are discussed in Section 4.

2 Methods

2.1 Model description

CLASSIC is the land surface component of the Canadian Earth System Model (CanESM) (Swart et al., 2019) and the open-source community model successor to CLASS-CTEM (Melton et al., 2020), which couples the physics (the Canadian Land Surface Scheme; CLASS; Verseghy (2017)) and biogeochemistry (the Canadian Terrestrial Ecosystem Model; CTEM; Arora (2003); Melton and Arora (2016)) sub-modules. The exchange of energy, water, momentum, and C at the land surface is represented in CLASSIC (for details see Melton et al. (2020)). The model is driven by seven atmospheric variables: air temperature (T_a), precipitation rate, air pressure, specific humidity (q), wind speed, and incoming shortwave and longwave radiation. Water and heat fluxes between the ground and the atmosphere, as well as its transfer between soil layers and snow, when present, are usually calculated on a half-hourly time step. The number of soil layers and their thicknesses can be chosen depending on the application, but typically CLASSIC uses 20 ground layers of increasing thicknesses starting with 10 layers of equal 10 cm thickness giving a maximum depth of 61.4 m. Heat transfer occurs within the whole ground column, including both soil and bedrock layers. The movement of water, however, is limited to the permeable soil layers. Canopy conductance and photosynthesis are calculated on the same time step as the energy and water fluxes while vegetation (leaf, stem, root), litter and soil C pools as well as respiratory fluxes are calculated on a daily time step. We prescribed the vegetation cover which is represented by plant functional types (PFTs) and their percent coverage (see Table 1). Vegetation biomass and height, LAI and rooting depths are dynamically determined within the biogeochemistry sub-module based upon photosynthesis and respiration, PFT-specific C allocation parameters and land surface characteristics (e.g., soil temperatures, soil moisture and net radiation) obtained from the physics sub-module. The physical land surface properties are calculated separately for up to four subareas of each grid cell (bare ground, snow-covered bare ground, vegetation over soil and vegetation over snow). In CLASSIC version 1.2 as used here, the vegetation, as seen by the physics submodule, is composed of five broad categories of PFTs (i.e., needleleaf trees, broadleaf trees, crops, grasses and shrubs). The biogeochemical calculations differentiate between evergreen and deciduous (split into cold and drought deciduous) PFTs and C_3 and C_4 photosynthetic pathways for crops and grasses, which results in 12 PFTs for the biogeochemistry sub-module.

2.2 Evapotranspiration parameterization and partitioning

The calculation of ET in CLASSIC and modifications made to its partitioning are described in detail in Appendix A. In short, ET is calculated as the sum of the components E_s, which originates from bare soil and the soil underneath the vegetation canopy, E_c and T. The potential evaporation rate from the soil depends on the ground evaporation efficiency (β; unitless; Equation A20), which is determined using an empirical formulation based on Lee and Pielke (1992) and Merlin et al. (2011). Based on simulations at flux tower sites, we determined that CLASSIC overestimates E_s and thus ET in sparsely vegetated arid or semi-arid regions (see Meyer et al. (2021); E_s and ET are not shown here, but the ET bias is comparable to the bias in LE in Figure B3). During the wet season, CLASSIC simulates excessive amounts of E_s, limiting the amount of moisture within the soil for the dry season, which causes a suppression of photosynthesis in these regions. In order to avoid excessive E_s from bare soil surfaces in CLASSIC, we implemented a process-based β parameterization building on the previously used empirical formulation (Merlin et al., 2011; Meyer et al., 2021). In the new formulation, E_s is determined by water vapour diffusion through a thin DSL whose thickness is calculated based on the moisture content of the top soil layer following Swenson and Lawrence (2014). This approach was chosen, as it is likely to have a stronger effect on E_s than a litter layer for example in sparsely-vegetated areas. The way the DSL parameterization was implemented also works well with CLASSIC's structure. In addition to the DSL's effects on E_s, we have implemented its effects on H and the ground heat flux (G) via the thermal conductivity, which depends on the degree of soil saturation (see Section A4 for details). Changes in surface albedo, when the DSL is present, were also accounted for (see Section A5). Available observations, although uncertain, indicate that CLASSIC also underestimates the global T/ET. To address this, we modified the partitioning of E_c and T, as in the original CLASSIC formulation T could only occur when there was no water on the canopy. The modified CLASSIC version allows the dry fraction of the canopy to transpire while E_c occurs from the wet canopy fraction following Fan et al. (2019) (see Section A6 for details).

2.3 Simulations

We performed simulations using CLASSIC v.1.2 with the original CEVAP formulation of soil evaporation (labelled 'Baseline'), a model version including the DSL parameterization (labelled 'DSL'; Section A3) and a version including both the DSL parameterization and a modified partitioning of E_c and T (labelled 'DSL-EcT'; Section A6) (see Table 1). Site-level simulations for a selection of sites (see Table 2) from the FLUXNET2015 dataset (Pastorello et al., 2020) were driven by observed meteorology at these sites. Site-specific information such as vegetation cover and composition, soil texture and depth were obtained from the literature (Melton et al., 2020). At these sites, CLASSIC was driven by cycling through the meteorological measurements available and the atmospheric CO_2 concentration from the first year of measurements at each site until the C pools reached equilibrium (defined as annual NEP / NPP ≤ 0.02, where NEP is the net ecosystem productivity and NPP is the net primary productivity). Then, CLASSIC was run for the years available at each site with transient atmospheric CO_2 concentrations from Le Quéré et al. (2018).

We also performed global simulations on the CanESM grid (approximately 2.8°by 2.8°). In order to assess differences between the CLASSIC versions and account for uncertainty in model forcing and geophysical inputs, simulations are driven by combina-

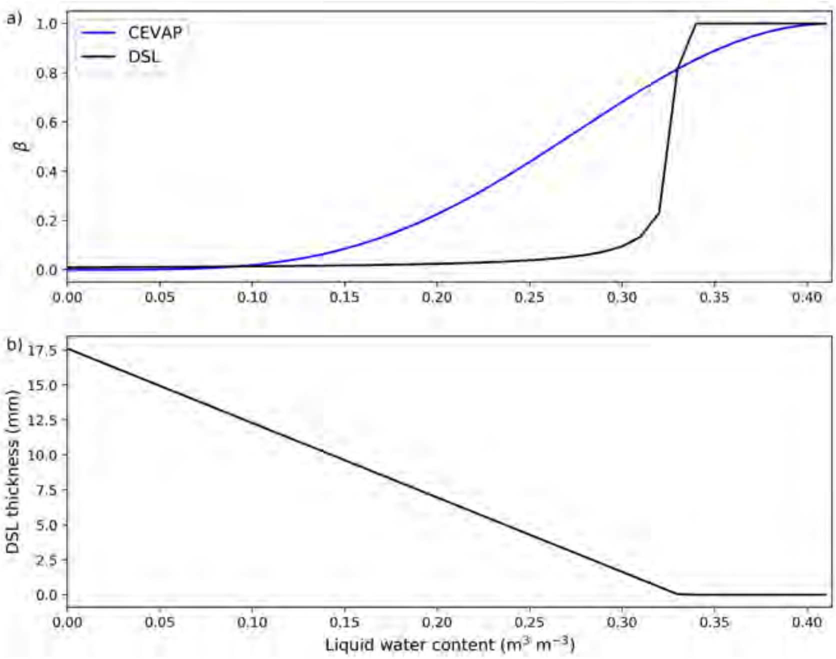

Figure 1: Soil evaporation efficiency (β) determined using the original CEVAP parameterization (Equation A20; blue line) as well as the calculation using the resistance due to the DSL (first term on the right hand side of Equation A19; black line) for liquid water content values of the top soil layer ranging between 0 and the soil porosity (set to 0.41 m^3 m^{-3} for this example) (a) and the thickness of the DSL for the respective liquid water content (b). This example was derived from annual average values of $C_{DH} \times v_a$, τ, and D_v from year 2005 at the US-Sta shrubland FLUXNET site (see Table 2).

Table 1: Calculation of the surface evaporation efficiency (β) and the canopy evaporation (E_c) and transpiration (T) components in the three CLASSIC versions (Baseline, DSL and DSL-EcT) used in this study as well as the meteorological forcing and land cover representations used in the simulations. The simulations, where the meteorological forcing and land cover are bold, are the ones shown in the geographic distributions and in Figure 5.

Simulation	**Surface evaporation efficiency**	**$E_c - T$ partitioning**	**Meteorological forcing**	**Land cover**
Baseline	CEVAP (Equation A20)	T only occurs, when the whole canopy is dry	**CRUJRAv2.2**	**ESACCI**
			GSWP3W5E5	ESACCI
			CRUJRAv2.2	GLC2000
			GSWP3W5E5	GLC2000
DSL	determined using DSL (Equation A19)	T only occurs, when the whole canopy is dry	**CRUJRAv2.2**	**ESACCI**
			GSWP3W5E5	ESACCI
			CRUJRAv2.2	GLC2000
			GSWP3W5E5	GLC2000
DSL-EcT	determined using DSL (Equation A19)	E_c occurs from wet canopy fraction, T from dry canopy fraction (Section A6)	**CRUJRAv2.2**	**ESACCI**
			GSWP3W5E5	ESACCI
			CRUJRAv2.2	GLC2000
			GSWP3W5E5	GLC2000

tions of two different meteorological forcing datasets and two different land cover representations, resulting in four simulations for each CLASSIC version. Meteorological forcing for the simulations was either provided by the Climate Research Unit Japanese 55-year reanalysis version 2.2 (CRUJRAv2.2, 1901-2020; CRU-JRA (2021); Harris et al. (2014, 2020); Kobayashi et al. (2015)) or the Global Soil Wetness Project Phase 3 (GSWP3) -WFDE5 over land merged with ERA5 over the ocean (W5E5) (GSWP3W5E5; 1901-2016; Lange (2020)). The methodology of Melton and Arora (2016) was used to disaggregate the 6-hourly meteorological data to the half-hourly time step CLASSIC uses. Model preparation for historical simulations included spinups that cycled through the meteorological forcings from 1700-1725 using constant CO_2 concentrations from 1700 until an equilibrium state was reached. Then, historical simulations with transient CO_2 concentrations, vegetation cover and composition, including the effects of land use change and fire, were performed from 1700-2019 (for CRUJRAv2.2) or 1700-2016 (for GSWP3W5E5). Two different land cover representations are used for the CLASSIC simulations, which are based on the Global Land Cover 2000 (GLC2000) and the European Space Agency Climate Change Initiative (ESACCI; ESA (2017)) datasets. As described in A. Wang et al. (2006), these datasets are mapped onto CLASSIC's PFTs and a timeseries including changes in crop area is created. While the site-level simulations can include all 12 PFTs described in 2.1, the global land cover representations used here do not include shrub PFTs and sedges, so they only include nine PFTs for the biogeochemical calculations and four PFTs (i.e., needleleaf trees, broadleaf trees, crops and grasses) for the physics.

2.4 Observation-based estimates of global T/ET

Global average estimates of the T/ET ratio have been reported by other studies and can be used to evaluate our model results. Techniques used to determine T/ET include isotopes, site measurements, remote sensing as well as a hybrid approach (Wei et al., 2017). As the water remaining after E is enriched in the heavier oxygen (^{18}O) and hydrogen (^{2}H) isotopes, whereas T does not change isotope ratios, measurements of oxygen and hydrogen stable isotope ratios can be used to partition T and E (Jasechko et al., 2013). Jasechko et al. (2013) used isotope measurements from Earth's large lakes and calculated lake catchment T from stable isotope mass balances between water inputs and losses. They then up-scaled their calculations to global T using a global freshwater stable isotope mass balance resulting in T/ET of 0.80-0.90 (25th and 75th percentiles) (Jasechko et al., 2013). Coenders-Gerrits et al. (2014), however, suggest that Jasechko et al. (2013)'s T/ET was overestimated and showed that using different inputs results in T/ET of 0.50-0.80 with a median value around 0.65. Further tests with different inputs and increased uncertainty estimates, decreased the median T/ET even further to 0.58 and increased its uncertainty with 25th and 75th percentiles of 0.35 and 0.8 (Coenders-Gerrits et al., 2014). Good et al. (2015) also comment that previous studies might have overestimated T/ET, as they neglected that E originates from multiple pools and did not account for their connectivity. Good et al. (2015) estimate the fraction of surface water that is bound in the soil and accessible by plants for T versus mobile water that quickly passes through the soil through preferential flow paths and is assumed to have the same isotopic composition as precipitation, as it does not mix with soil water. Good et al. (2015) determined the global terrestrial isotope budget using an isotope mass balance approach, gridded land-atmosphere water fluxes and an estimate of the soil water-surface water connectivity resulting in T/ET between 0.56 and 0.74 (25th and 75th percentiles) and a mean of 0.64. A compilation of site-level measurements of T and ET in different ecoregions using a range of techniques (eddy covariance, sap flow or isotopic approaches in combination with biophysical models to partition ET) found a global mean T/ET of 0.61 $\pm$ 0.15 ($\pm$ 1 SD) (Schlesinger & Jasechko, 2014). L. Wang et al. (2014) showed that site-level T/ET ranged from 0.38 to 0.77 (25th and 75th percentiles) and that 43% of the variations in T/ET could be explained by differences in LAI and the growing stage of the ecosystem. The remote sensing-based global T/ET estimates used to evaluate CLASSIC (Section 3.2) were obtained from studies using remotely sensed datasets of meteorological variables (e.g., radiation, air temperature, precipitation) and vegetation characteristics to drive different ET algorithms, which included the Penman-Monteith model (PM-MOD; Q. Mu et al. (2007, 2011)), the Global Land Evaporation Amsterdam Model (GLEAM; Miralles et al. (2011)), the Priestley-Taylor Jet Propulsion Laboratory (PT-JPL; Fisher et al. (2008)) model (Miralles et al., 2016) and the Penman-Monteith-Leuning

Table 2: FLUXNET sites from the FLUXNET2015 dataset used in this study.

Site ID	Site name	Latitude	Longitude	Elevation	Years	IGBP code	DOI
AU-Tum	Tumbarumba	35.6566	148.1517	1200	2001–2013	EBF	https://doi.org/10.18140/FLX/1440126
BR-Sa1	Santarem-Km67-Primary Forest	2.8567	54.9589	88	2002–2011	EBF	https://doi.org/10.18140/FLX/1440032
CA-DL1	Daring Lake - Mixed Tundra	64.8689	-111.5748	425	2004-2017	OSH	https://doi.org/10.5281/zenodo.4301133
CA-Qfo	Quebec – E. Boreal, Mature Black Spruce	49.6925	74.3421	382	2003–2010	ENF	https://doi.org/10.18140/FLX/1440045
CA-TPD	Ontario – Turkey Point Mature Deciduous	42.6353	80.5577	260	2012–2014	DBF	https://doi.org/10.18140/FLX/1440112
CG-Tch	Tchizalamou	4.2892	11.6564	82	2006–2009	SAV	https://doi.org/10.18140/FLX/1440142
CN-Dan	Dangxiong	30.4978	91.0664	4313	2004–2005	GRA	https://doi.org/10.18140/FLX/1440138
CZ-BK1	Bily Kriz forest	49.5021	18.5369	875	2004–2014	ENF	https://doi.org/10.18140/FLX/1440143
DE-Kli	Klingenberg	50.8931	13.5224	478	2004–2014	CRO	https://doi.org/10.18140/FLX/1440149
DE-Tha	Tharandt	50.9624	13.5652	385	1996–2014	ENF	https://doi.org/10.18140/FLX/1440152
DK-Sor	Sorø	55.4859	11.6446	40	1996–2014	DBF	https://doi.org/10.18140/FLX/1440155
DK-ZaH	Zackenberg Heath	74.4733	-20.5545	38	2000-2014	GRA	https://doi.org/10.18140/FLX/1440224
FI-Hyy	Hyytiälä	61.8474	24.2948	181	1996–2014	ENF	https://doi.org/10.18140/FLX/1440158
FR-Fon	Fontainebleau-Barbeau	48.4764	2.7801	103	2005–2014	DBF	https://doi.org/10.18140/FLX/1440161
FR-Pue	Puéchabon	43.7413	3.5957	270	2000–2014	EBF	https://doi.org/10.18140/FLX/1440164
ES-Amo	Amoladeras	36.8336	-2.2523	58	2008-2012	OSH	https://doi.org/10.18140/FLX/1440156
ES-LgS	Laguna Seca	37.0979	2.9658	2267	2007–2009	OSH	https://doi.org/10.18140/FLX/1440225
ES-LJu	Llano de los Juanes	36.9266	-2.7521	1600	2004-2013	OSH	https://doi.org/10.18140/FLX/1440157
GF-Guy	Guyaflux (French Guiana)	5.2788	52.9249	48	2004–2014	EBF	https://doi.org/10.18140/FLX/1440165
GH-Ank	Ankasa	5.2685	2.6942	124	2011–2014	EBF	https://doi.org/10.18140/FLX/1440229
IT-Lav	Lavarone	45.9562	11.2813	1353	2003–2014	ENF	https://doi.org/10.18140/FLX/1440169
IT-SRo	San Rossore	43.7279	10.2844	6	1999–2012	ENF	https://doi.org/10.18140/FLX/1440176
IT-Tor	Torgnon	45.8444	7.5781	2160	1999–2012	GRA	https://doi.org/10.18140/FLX/1440237
MY-PSO	Pasoh Forest Reserve	2.9730	102.3062	147	2003–2009	EBF	https://doi.org/10.18140/FLX/1440240
NL-Loo	Loobos	52.1666	5.7436	25	1996–2014	ENF	https://doi.org/10.18140/FLX/1440178
PA-SPs	Sardinilla-Pasture	9.3138	79.6314	68	2007–2009	GRA	https://doi.org/10.18140/FLX/1440179
RU-Che	Cherski	68.6130	161.3414	6	2002–2005	WET	https://doi.org/10.18140/FLX/1440181
RU-Fyo	Fyodorovskoye	56.4615	32.9221	265	1998–2014	ENF	https://doi.org/10.18140/FLX/1440183
RU-Ha1	Hakasia steppe	54.7252	90.0022	446	2002–2004	GRA	https://doi.org/10.18140/FLX/1440184
RU-SkP	Yakutsk Spasskaya Pad larch	62.2550	129.1680	246	2012–2014	DNF	https://doi.org/10.18140/FLX/1440243
SD-Dem	Demokeya	13.2829	30.4783	500	2005–2009	SAV	https://doi.org/10.18140/FLX/1440186
US-MMS	Morgan Monroe State Forest	39.3232	-86.4131	275	1999-2014	DBF	https://doi.org/10.18140/FLX/1440083
US-SRC	Santa Rita Creosote	31.9083	-110.8395	950	2008-2014	OSH	https://doi.org/10.18140/FLX/1440098
US-Sta	Saratoga	41.3966	-106.8024	2069	2005-2009	OSH	https://doi.org/10.18140/FLX/1440115
US-WCr	Willow Creek	45.8059	90.0799	520	1999–2014	DBF	https://doi.org/10.18140/FLX/1440095
US-Whs	Walnut Gulch Lucky Hills Shrub	31.7438	-110.0522	1370	2008-2014	OSH	https://doi.org/10.18140/FLX/1440097
US-Wkg	Walnut Gulch Kendall grasslands	31.7365	109.9419	1531	2004–2014	GRA	https://doi.org/10.18140/FLX/1440096
ZA-Kru	Skukuza	25.0197	31.4969	359	2000–2013	SAV	https://doi.org/10.18140/FLX/1440188
ZM-Mon	Mongu	15.4378	23.2528	1053	2007–2009	DBF	https://doi.org/10.18140/FLX/1440189

IGBP land classification abbreviations used include evergreen broadleaf forest (EBF), evergreen needleleaf forest (ENF), savanna (SAV), deciduous broadleaf forest (DBF), grassland (GRA), cropland (CRO), open shrubland(OSH), closed shrubland (CSH), permanent wetland (WET), and deciduous needleleaf forest (DNF).

(PML; Y. Zhang et al. (2016)) model. Of the remote-sensing-based global ET models, PM-MOD is one of the most widely used (for example in the MODIS ET product MOD16). Unlike other Penman-Monteith-based models, PM-MOD determines the surface and aerodynamic resistances without using soil moisture or wind speed inputs. Its resistance parameters have, however, been calibrated using EC towers, which is not required for GLEAM and PT-JPL (Miralles et al., 2016). GLEAM determines the ET components based on Priestley and Taylor (1972) apart from interception losses, which use Gash (1979)'s analytical model driven by precipitation observations (Miralles et al., 2016). Despite using the same forcing datasets to drive PM-MOD, GLEAM and PT-JPL, where input requirements overlapped, differences in modelled ET and its component fluxes were large (Miralles et al., 2016). Compared to the other two models and data from ERA-Interim reanalysis (Dee et al., 2011) and the model tree ensemble (MTE; Jung et al. (2009, 2010)) product, which uses a machine-learning algorithm trained on FLUXNET data, PM-MOD tends to underestimate ET, especially in the tropics and dry subtropical regions, apart from in the Northern high-latitudes (Miralles et al., 2016). In high latitudes, GLEAM and PT-JPL had lower ET than PM-MOD likely due to deficiencies in the Priestley-Taylor approach when available energy is low (Miralles et al., 2016). Partitioning of ET into E_s, E_c and T largely differs between the models with T being much lower in PM-MOD and E_s and E_c higher than in the other two models (Miralles et al., 2016). PM-MOD's T/ET of 0.24 is an outlier compared with the other observation-based estimates (see Section 3.2), which might in part be due to its underestimation of ET in the tropics and dry sub-tropics, which tend to contribute the most to global T (Schlesinger & Jasechko, 2014). PM-MOD also shows relatively high E_s in tropical regions, where GLEAM and PT-JPL show very little E_s. E_c's contribution to ET is also much larger on average in PM-MOD with 24% compared to 18% in PT-JPL and 10% in GLEAM (Miralles et al., 2016) and PML (Y. Zhang et al., 2016).

3 Results

3.1 Site-level results

Baseline CLASSIC simulations at a selection of FLUXNET sites (Table 2) showed an overestimation of LE compared with eddy covariance measurements at sparsely vegetated sites such as open shrublands (e.g., ES-Amo, ES-LJu, US-Sta) during wet periods and an underestimation of LE during the peak growing season or drier periods at these sites (Figure 2 and B3). During wet periods, when LE was overestimated, H was underestimated (Figure B4). During dry periods, on the other hand, H was overestimated compared to observations. The ground heat flux (G; Figure B5) also tended to be overestimated at these sites, especially during summer. The overestimation of LE led to a strong reduction in soil moisture in the top layer (Figure B6). Thus, GPP was reduced and underestimated during the peak growing season at several open shrubland or grassland sites (e.g., ES-LJu, US-SRC, ES-Amo; Figure 2 and B2).

The DSL simulations mainly affected LE with statistically significant (t-test, $p < 0.01$) differences between the bias in the DSL simulation and the bias in the Baseline simulation (Figure B8) at sparsely vegetated sites such as open shrubland sites with a large bare ground area (e.g., ES-Amo, ES-LgS, ES-LJu, US-Sta, US-SRC, US-Whs), where the DSL parameterization reduced LE during wet periods and increased LE during dry periods (Figure 2 and B3). Thus, the DSL simulations eliminated or reduced overestimation of LE during wet times and the simulated seasonal cycle of LE more closely represented observations at these sites. The reduction in LE in the wet season led to an increase in soil moisture of the top layer (Figure B6) and thus to higher GPP later in the year (Figure 2 and B2). At the majority of sites, G was only minimally affected (Figure B5).

The DSL-EcT modifications affected LE at both sparsely vegetated sites as well as sites with high LAI (e.g., evergreen forest sites; Figures 2, B3, B7 and B8). As in the DSL simulations, LE at the sparsely vegetated sites was reduced during wet periods and increased during dry periods due to the DSL parameterization (Figure 2). Effects of the E_c and T partitioning modifications on LE at the open shrubland sites were minor, while LE at densely vegetated sites such as tropical forests in Brazil (BR-Sa1) or French Guiana (GF-Guy) was more strongly impacted (Figure B3). At the sites where LE increased in the DSL-EcT simulations (mainly denser forest sites), H decreased (Figure B4). For the more sparsely-vegetated sites, on the other hand, H slightly increased, especially during wetter periods. The effect on G at each site was minimal (Figure B5). The E_c and T partitioning modifications resulted in slightly lower GPP than for the DSL simulation, as LE increased and the liquid water content of the top soil layer ($\theta_{l,1}$) decreased.

Biases in simulated daily LE and GPP compared to observations for the FLUXNET sites were reduced in the DSL and DSL-EcT simulations compared to the Baseline simulations at several of the sites (Figure 3 and 4). Averaged over all the sites, the mean absolute error (MAE) and root mean square error (RMSE) in LE were reduced in the DSL-EcT simulations compared to the Baseline with a decrease in mean MAE of 5% and in mean RMSE of 4% (Figure 3). T-tests showed that the majority of sites showed statistically significant differences ($p < 0.01$) between daily simulated and observed LE and GPP for all model configurations (Figure 3 and 4). The magnitude of reduction in MAE and RMSE varied between sites.

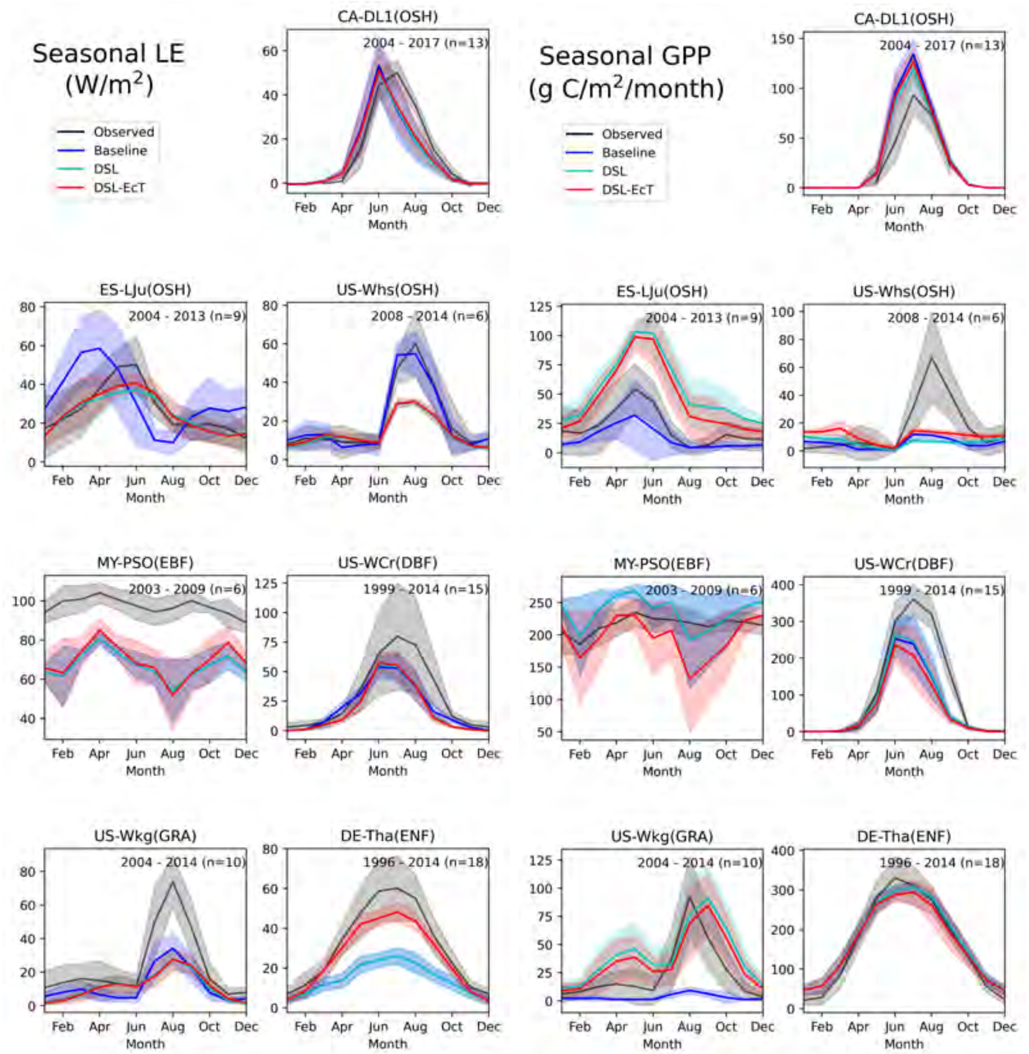

Figure 2: Monthly mean observed and simulated latent heat flux (LE) and gross primary productivity (GPP) for a selection of FLUXNET sites (showing different biomes and climates) for the Baseline, DSL and DSL-EcT simulations (Table 1). All sites are shown in Figures B2 and B3. The shading shows the standard deviation over the available years. Site names, their biomes and years of measurements used are listed for each site (for more details see Table 2). For some sites, the results from the different simulations and observations are overlapping and lines may be difficult to distinguish.

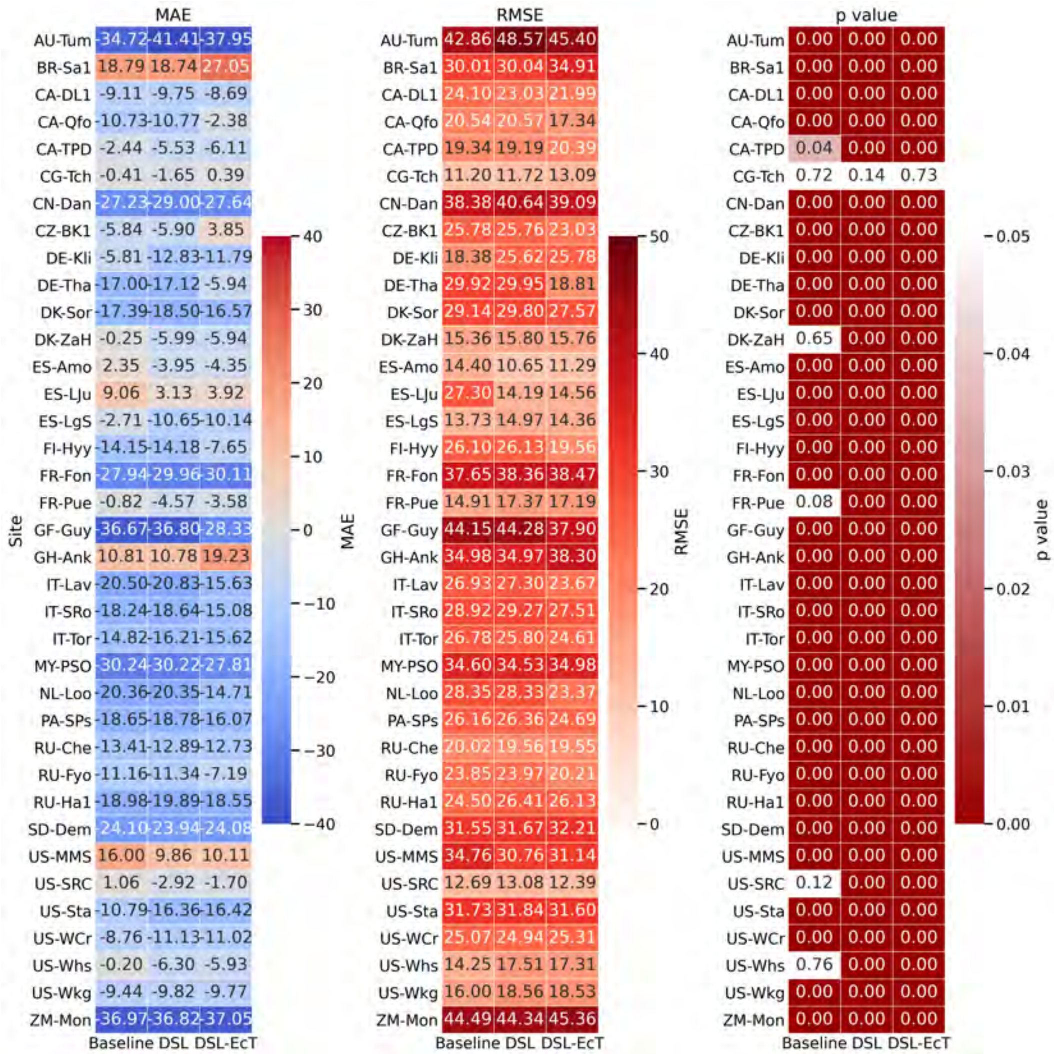

Figure 3: Mean absolute error (MAE, W m^{-2}), root mean square error (RMSE, W m^{-2}) and p value (determined using an independent two-sided t-test) between the observed and simulated daily latent heat flux (LE) for the FLUXNET sites (Table 2) for the Baseline, DSL and DSL-EcT simulations (Table 1). For MAE and RMSE, values closer to zero indicate better model performance.

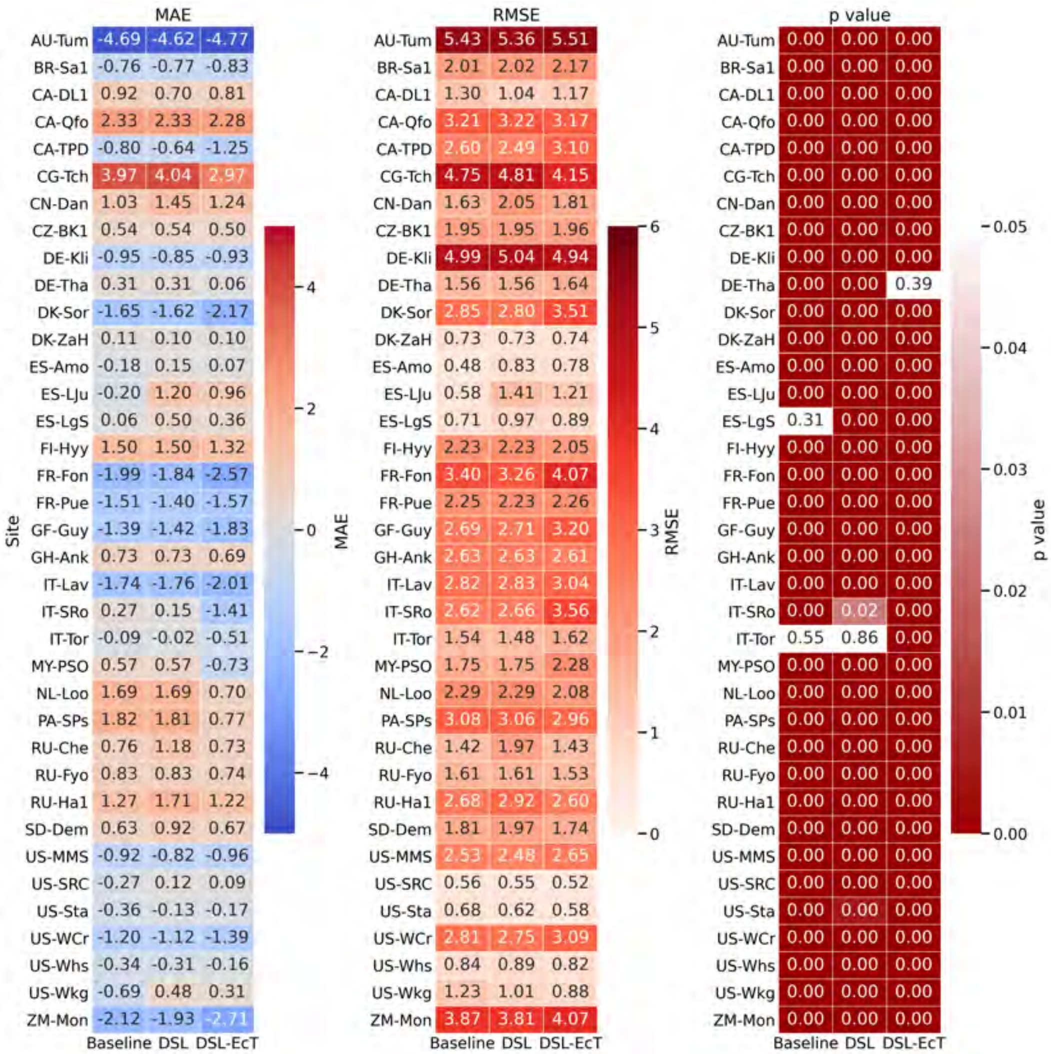

Figure 4: Mean absolute error (MAE, g C m^{-2} day^{-1}), root mean square error (RMSE, g C m^{-2} day^{-1}) and p value (determined using an independent two-sided t-test) between the observed and simulated daily gross primary productivity (GPP) for the FLUXNET sites (Table 2) for the Baseline, DSL and DSL-EcT simulations (Table 1). For MAE and RMSE, values closer to zero indicate better model performance.

3.2 Global results

For the baseline CLASSIC simulations, the largest contribution to global ET comes from E_s (39.5%), followed by E_c (34.6%) and T (25.9%) (Figure 5). Results shown in Figure 5 focus on simulations using one land cover and one meteorological forcing dataset as the results were similar across the simulations using different land cover and meteorological forcing. The ET partitioning in baseline CLASSIC results in a lower T/ET ratio than estimates from isotope, remote sensing (apart from the PM-MOD algorithm, which is an outlier compared to other remote sensing-based estimates as discussed in Section 2.4) or site measurements as well as several other process-based models suggest (Figure 6). Total global GPP, LE and H are within the uncertainty bounds of observation-based estimates (Figure C1a-f). Low productivity regions such as the southwestern United

States, southern Australia, southern South America, however, show very low to zero GPP. Due to the low GPP, E_s exceeds E_c and T in these regions (not shown).

Implementing the DSL parameterization changes CLASSIC's ET partitioning by significantly reducing E_s (t-test, $p < 0.01$) and increasing E_c (t-test, $p = 0.013$) and T (t-test, $p < 0.01$) compared to baseline CLASSIC (Figure 5). As T increased and ET decreased, global T/ET significantly increased (t-test, $p < 0.01$) from $\sim$0.25 on average (taken across the simulations listed in Table 1) in baseline CLASSIC to $\sim$0.30 in the DSL simulations (Figure 6). Slightly increased T in the DSL simulations was due to an increase in GPP, especially in arid and semi-arid regions, where E_s was reduced and soil moisture available to the vegetation increased.

Combining the DSL parameterization with the modifications to E_c and T partitioning resulted in slightly increased ET (t-test, $p < 0.01$), a reduction in E_s (t-test, $p < 0.01$), a slight decrease in E_c (t-test, $p < 0.01$) and an increase in T (t-test, $p < 0.01$) (Figure B9). Thus, the T/ET ratio is significantly higher (t-test, $p < 0.01$) for the DSL-EcT simulations than the CEVAP simulations by 0.15 - 0.17 depending on the land cover and meteorological forcing (Table B1 and Figure 5). The DSL-EcT modifications decreased both E_s and E_c while increasing T (all statistically significant, t-test, $p < 0.01$). Despite differences in the water fluxes between simulations using the different forcings (see Figure B9 and Section 2.3), the modified CLASSIC versions changed ET and its partitioning more than the different forcing datasets did (Figure 5 and Table B1). The T/ET for the DSL-EcT simulations remained lower than several observation-based estimates using isotopes, other site measurements or remote sensing algorithms (except PM-MOD) suggest, but was closer to estimates from other models and is close to the CMIP5 ensemble mean value of 0.41 (Lian et al., 2018).

As CLASSIC's T/ET remained low compared to observations and some other LSMs, we considered further options to improve its ET partitioning. Lian et al. (2018) suggested that the simulation of T/ET in ESMs could be improved by taking into account the diffuse fraction of incoming radiation, as it would affect the photosynthetic activity of shaded leaves and likely increase T. Including the diffuse radiation fraction using a 2-leaf photosynthesis scheme instead of the big-leaf scheme in CLASSIC (Arora, 2003), however, only had minor impacts on T and T/ET. Both increased by $\sim$2%, respectively, compared to the big-leaf scheme without the diffuse radiation fraction in CLASSIC resulting in T/ET of 0.427 driven with CRUJRA and ESACCI.

GPP significantly increased (t-test, $p < 0.01$) in arid and semi-arid regions such as the southwestern United States and Australia due to the modifications in ET partitioning while some densely vegetated areas (especially in the Tropics) showed a reduction in GPP (Figure 7b). The majority of the regions where GPP increased in the DSL-EcT simulations showed an increase in H and a small reduction in LE (Figure 7d and f) or ET, as the decrease in E_s (Figure 8b) exceeded the increases in E_c and T (Figure 8d and f). In areas with reduced GPP, H decreased and LE (Figure 7b, d and f) and ET tended to increase, as E_s increased or decreased only slightly, E_c decreased moderately and T increased statistically significantly (t-test, $p < 0.01$; Figure 8d and f). In tropical forests (here defined as areas between 25°S and 25°N with a leaf area index > 3 $m^2\ m^{-2}$), the DSL-EcT simulation mainly affects E_c and T while the change in E_s is relatively small. In semi-arid regions, on the other hand, E_s and T are more strongly affected than E_c.

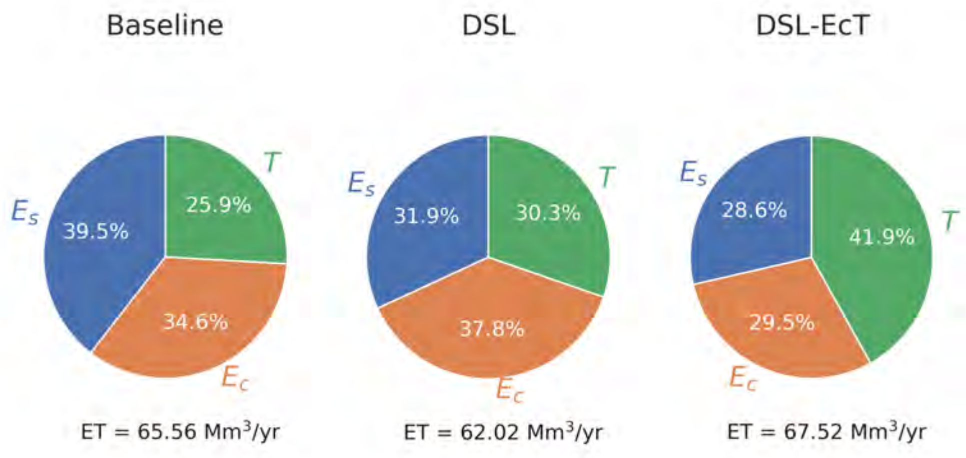

Figure 5: Partitioning of evapotranspiration (ET) into its components soil evaporation (E_s), canopy evaporation (E_c) and transpiration (T) for the three different CLASSIC versions (see Section 2.3; Table 1). Percentages of E_s, E_c and T are global averages over 1997-2016 for simulations using the CRUJRA meteorological forcing and the ESACCI land cover. Total ET values for the different CLASSIC versions are shown below the pie charts.

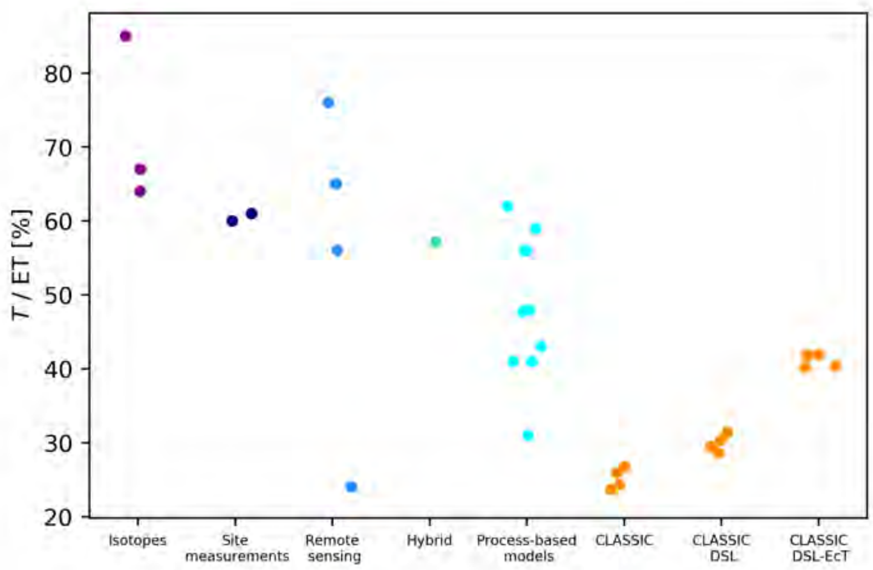

Figure 6: Globally averaged T/ET from observation-based datasets (see Section 2.4) and different land surface or Earth System models (adapted from Wei et al. (2017)) alongside the versions of CLASSIC tested in our study (see Section 2.3) . The "Hybrid" reference dataset uses site measurements, satellite-based observations, as well as land surface model (a complex physically based model i.e., the Community Land Model 4.5, the remote sensing-based Global Land Evaporation Amsterdam Model (GLEAM) and a simple biophysical model i.e., Penman-Monteith-Leuning Model; PML) outputs, to upscale site-level measurements of the ET components (Wei et al., 2017). For each of the CLASSIC versions (Table 1), the four points represent the results using a combination of the two different meteorological forcing datasets and the two land cover representations (Section 2.3). The horizontal displacement of the dots is just to allow each one to be visible.

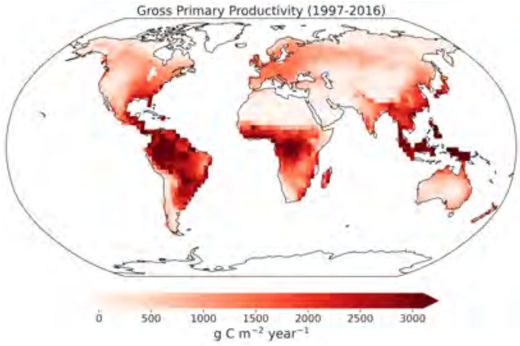

(a) DSL-EcT

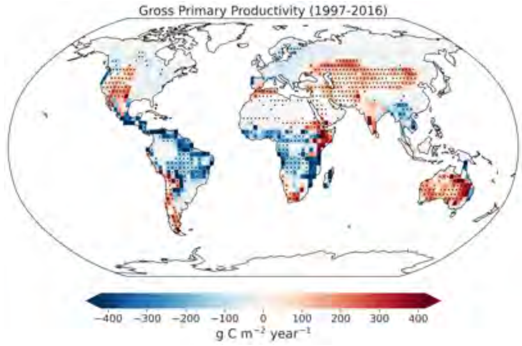

(b) DSL-EcT - Baseline

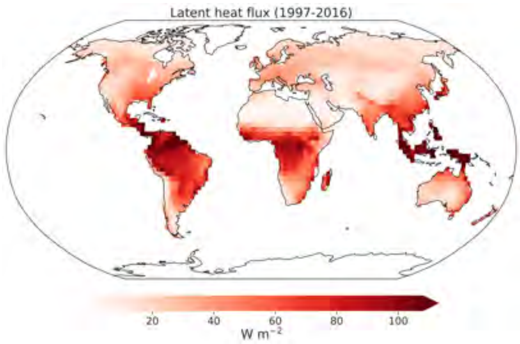

(c) DSL-EcT

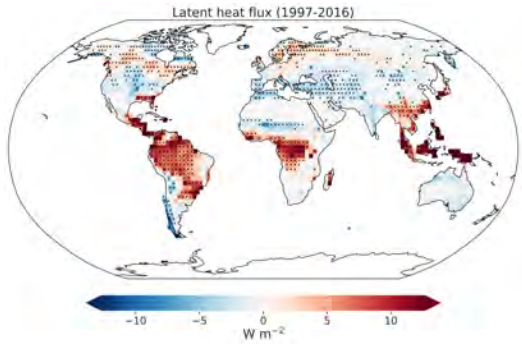

(d) DSL-EcT - Baseline

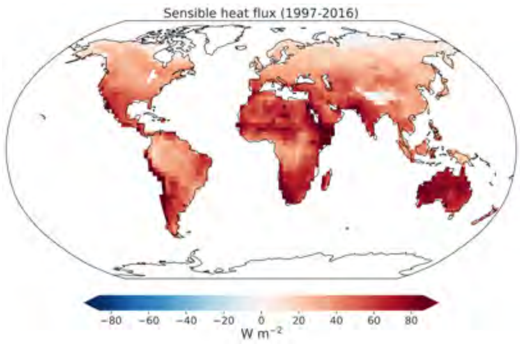

(e) DSL-EcT

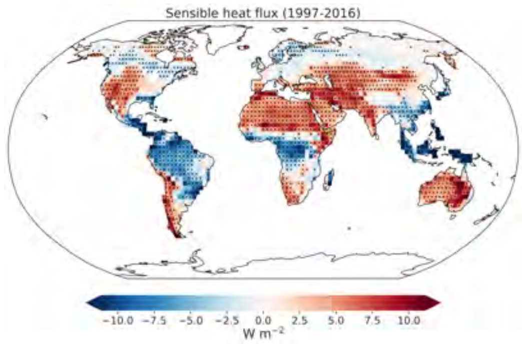

(f) DSL-EcT - Baseline

Figure 7: Geographic distribution of annual gross primary productivity (GPP), latent (LE) and sensible (H) heat flux averaged over 1997-2016 for the DSL-EcT simulation (a, c, e) and the difference between the DSL-EcT and Baseline simulations (b, d, f) using the CRUJRA meteorological forcing and the ESACCI land cover. Grid cells with dots indicate that differences are statistically significant (independent two-sample t-test p level $<$ 0.01).

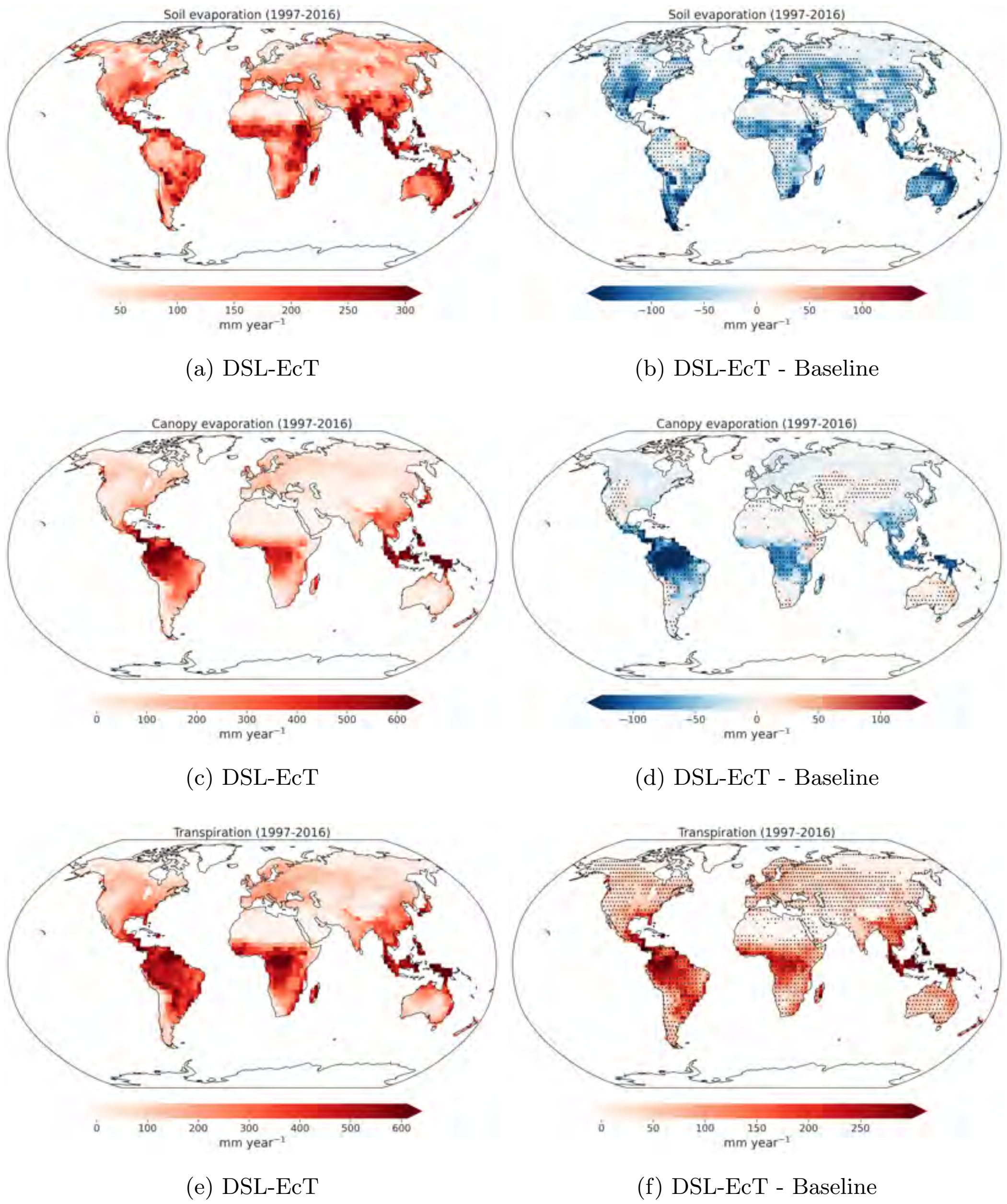

(a) DSL-EcT (b) DSL-EcT - Baseline

(c) DSL-EcT (d) DSL-EcT - Baseline

(e) DSL-EcT (f) DSL-EcT - Baseline

Figure 8: Geographic distribution of soil evaporation (E_s), canopy evaporation (E_c) and transpiration (T) averaged over 1997-2016 for the DSL-EcT simulation (a, c, e) and the difference between the DSL-EcT and Baseline simulations (b, d, f) using the CRUJRA meteorological forcing and the ESACCI land cover. Grid cells with dots indicate that differences are statistically significant (independent two-sample t-test p level < 0.01)

Parameter values which determine the DSL thickness (z_{max} and K; Equations A12 and A13) and the interception capacity of the canopy (the maximum storage of liquid water; p_l, Equation A31) are uncertain. To investigate how the chosen parameter values impact simulated energy fluxes and GPP, we conducted a sensitivity analysis with global simulations. The simulations demonstrated that LE has the opposite response to H and GPP as K, z_{max} and p_l are changed (Figure 9). Changing K or p_l affected LE,

H and GPP more than changes in z_{max}. Of the ET components, E_s is most affected by changes in K and z_{max}, while changes in p_l affected E_c the most. Changes in ET partitioning due to a modified p_l were relatively small, however. A reduction in p_l by 50% from 0.2 kg m^{-2} to 0.1 kg m^{-2} reduced E_c/ET only by 15% and increased E_s/ET and T/ET by 7% and 6%, respectively. Thus, even with a significantly reduced interception capacity, CLASSIC simulated an E_c that still contributed 25% of ET, which is higher than GSWP-2 (16%) (Dirmeyer et al., 2006) and CLM4 (20%) (D. M. Lawrence et al., 2011), while T was 44% of ET.

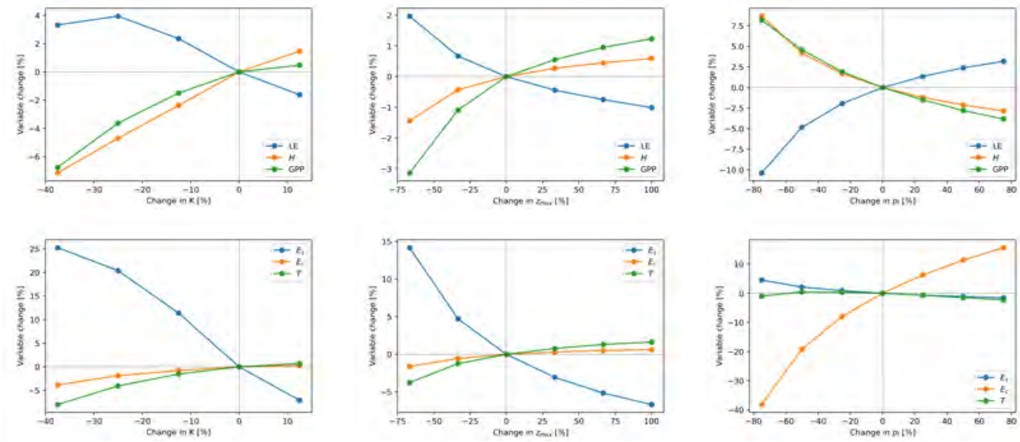

Figure 9: Percentage change in LE, H and GPP (top) and in E_s, E_c and T (bottom) with change in the parameters K, maximum DSL thickness (z_{max}) and the maximum storage of liquid water (p_l) in the sensitivity simulations performed using CLASSIC with the DSL-EcT configuration.

4 Discussion

The original CLASSIC version had unreasonably low T/ET compared to most observation-based estimates (see Section 2.4 and Figure 6) and other LSMs with a global mean value of 0.25 ± 0.01 (mean ± standard deviation of the ensemble of four simulations using two meteorological forcings and two land cover representations; Table B1). Similar to results of Swenson and Lawrence (2014) using the Community Land Model (CLM), implementing a DSL parameterization in CLASSIC increased the resistance to E_s, improved simulated ET and increased productivity in arid / semi-arid regions (Figures 2 and 7b). In areas, where the original β formulation (Equation A20) simulated high E_s, which reduced soil moisture availability later in the growing season, the DSL parameterization generally improved simulated LE and increased GPP, as there was more water available in the root zone (Figures 2 and B6). This agrees with findings in other studies using different models such as Swenson and Lawrence (2014) (CLM4.5) and Decker et al. (2017) (CABLE). Inclusion of a DSL parameterization alone increased CLASSIC's global T/ET to 0.30 ± 0.01 from 0.25 ± 0.01 in baseline CLASSIC. A further modification which influences the canopy fluxes, E_c and T, allowed T to occur from the dry portion of the canopy while intercepted water is evaporating from the wet canopy fraction. This change increased CLASSIC's global T/ET further to a value of 0.41 ± 0.01. This value is lower than observation-based global estimates of 0.57 ± 0.07 (Wei et al., 2017), but it equals the CMIP5 ensemble mean (Lian et al., 2018) and is 0.16 higher than the baseline CLASSIC simulations. Other models have been working on improving their T/ET ratio. For example, implementation of a bare soil resistance term for dry soils in the ORganizing Carbon and Hydrology in Dynamic EcosystEms (ORCHIDEE) LSM increased simulated T/ET at semi-arid shrub, grass and forest sites in the Southwestern US (MacBean et al., 2020). In the Community Atmosphere Biosphere Land Exchange (CABLE) model, T/ET at several FLUXNET sites was increased from an average value of 0.28 (ranging from 0.08 to 0.71 depending on the site) to 0.70 (ranging from 0.29 to 0.84) by implementing pore-scale-based resistance formulations of E_s, which reduced overestimation of E_s (Decker et al., 2017). In CLM, global T/ET has been increased from 0.43 in CLM3.5, to 0.48 in CLM4, which rises to 0.56 when the nitrogen (N) cycle is explicitly simulated, as ground evaporation decreased from 39% to 32% and 23%, respectively (D. M. Lawrence et al., 2011). To accomplish these increases in T/ET from CLM3.5 to CLM4 new litter resistance and canopy turbulence functions were added, which increased the resistance to ground E when litter was present and turbulent exchange was reduced under dense canopies. The differences in T/ET for the two versions of CLM4 (with and without the N cycle) are likely due to a higher LAI with the N cycle explicitly simulated, which increased T and E_c and reduced E_s (D. M. Lawrence et al., 2011). Our simulations with the modified DSL-EcT CLASSIC, which had higher T and T/ET than the baseline CLASSIC, changed LAI regionally, showing a statistically significant (t-test, p value < 0.01) increase in LAI in arid/semi-arid regions and a decrease in some tropical forests. Global mean LAI, however, did not appreciably change compared to the baseline CLASSIC and is higher than AVHRR and MODIS observations suggest in both simulations (Figure C1g and h). Comparing the CLASSIC DSL-EcT against CLM4 (no N cycle) (D. M. Lawrence et al., 2011) show CLASSIC DSL-EcT to have lower T (48% CLM4, 41% CLASSIC DSL-EcT), similar E_s (32% CLM4, 30% CLASSIC DSL-EcT) and higher E_c (20% CLM4, 29% CLASSIC DSL-EcT). The Global Soil Wetness Project Phase 2 (GSWP-2) multi-model mean (including thirteen land surface models; see Dirmeyer et al. (2006)) contributions to ET were 48% T, 36% E_s and 16% E_c (Dirmeyer et al., 2006). Variability between global estimates of the ET components from CLM4, GSWP-2 and other models such as GLEAM, PT-JPL and PM-MOD (Miralles et al., 2016) is large and uncertainties are high (see Section 2.4). Compared against observation-based estimates and other models, however, E_c remains too high in CLASSIC DSL-EcT while T is too low. As our parameter sensitivity tests (Section 3.2 and Figure 9) showed, the higher E_c is in part due to a higher maximum storage of liquid water (p_l) compared with CLM4 and a lower p_l of 0.1 kg m^{-2} would reduce CLASSIC's E_c to ∼25% of ET from 29%. Measurements of maximum water storage per leaf area index show large variability depending on the ecosystem, vegetation species and stand age with values ranging from 0.14 to 0.88 mm (Hadiwijaya et al., 2021), which suggest that a p_l of 0.1 kg m^{-2} could be too low.

In order to improve the simulation of the different ET components and especially T/ET in LSMs or ESMs, further processes have been highlighted as potentially important in other studies using different models. Chang et al. (2018) found that simulated T/ET of a subhumid, mountainous catchment improved when an empirical resistance formulation to E was replaced by a process-based soil surface resistance parameterization, and lateral flow, redistributing precipitation in mountainous terrain, was included in a process-based ecohydrological model. Here, we have included a process-based surface resistance parameterization through the simulation of the DSL, however, terrain-driven lateral flow is not included in CLASSIC. Its inclusion could improve T/ET further, as lateral flow affects soil moisture along hillslopes resulting in drier surfaces on upper slopes suppressing E more than T (Chang et al., 2018). Water redistribution in semi-arid ecosystems, however, is complex and in addition to lateral flow, local microtopography and biocrusts forming on bare soils can affect runoff and channel water to vegetated patches, where it infiltrates more easily and increases productivity (Chen et al., 2013; Rodríguez-Caballero et al., 2018). Another issue observed in LSMs is that root growth and distribution and interactions between soil moisture and root dynamics are often not adequately represented (Chang et al., 2018; P. Wang et al., 2018). P. Wang et al. (2018) showed that a dynamic root scheme combined with the simulation of the ground water table implemented in the Noah LSM, where root dynamics depend on fluctuating groundwater levels, improves simulation of root water uptake and latent heat fluxes in arid or semi-arid regions. During growing season periods when the water table declines, roots extract water from the saturated zone or directly from groundwater. In forests with deep roots, for example, ground water dynamics can impact energy, water and carbon fluxes as well as simulated soil moisture (De Pue et al., 2022; MacBean et al., 2020; Decharme et al., 2019). Including groundwater recharge from an aquifer in Niu et al. (2007) was shown to increase soil moisture and ET especially in transition areas from arid to wet regions (e.g., riparian zones in arid regions). The simulation of seasonal drought effects in LSMs or ESMs was found to be improved by combining the representation of groundwater replenishment from an aquifer with lateral flow and dynamic root distributions instead of commonly used static, prescribed root profiles (P. Wang et al., 2018). Uncertainties in pedotransfer functions, which are used to determine soil physical properties, also affect the ability of LSMs to adequately represent soil moisture (De Pue et al., 2022). Simulated soil moisture and infiltration might be improved by incorporating improved pedotransfer functions (Gupta et al., 2021; Pinnington et al., 2021), which depend on climatology and land use in addition to soil texture (Fatichi et al., 2020; Vereecken et al., 2019). Simulated drought response can also be improved by implementing a plant hydraulics scheme, which determines g_c based on xylem hydraulics instead of using an empirical moisture stress function (Eller et al., 2018). Especially under extreme climatic conditions or a changing climate, process-based models of g_c can improve simulated water fluxes during droughts. Eller et al. (2018) showed that their hydraulics-based g_c model was able to better represent effects of drought on T of tropical forests during El Niño events than an empirical drought scheme.

Future work, which would likely improve ET partitioning in CLASSIC and simulated T/ET, could include the representation of terrain-dependent lateral flow, plant hydraulics and possibly modifications to canopy interception such as inclusion of wind-driven loss of intercepted water or snow which increases throughfall (Véliz-Chávez et al., 2014). As Dong et al. (2022) attributed a warm bias in the central US in CMIP6 models, which CanESM exhibits as well, to low ET and T/ET, we are also planning to investigate the effects of the DSL and E_c-T partitioning modifications in the ESM CanESM to determine their effects on land C and water fluxes as well as the climate, when the land and the atmosphere interact.

5 Conclusions

LSMs often show poor ET partitioning with positive biases in E and negative biases in T, resulting in an underestimation of T/ET (Chang et al., 2018; Lian et al., 2018). These biases impact the simulation of C cycle processes. For example, we found that overestimation of E_s during periods of high soil moisture in sparsely vegetated areas such as low-latitude shrublands resulted in excessive plant water stress during the growing season and depressed GPP in CLASSIC simulations. To address CLASSIC's bias in E_s, we implemented a dry surface layer (DSL) parameterization that increases the surface resistance to water vapour and heat fluxes. To further improve simulated T, T is now allowed to occur from the dry fraction of the plant canopy at the same time as water evaporates from the wet fraction, which previously did not allow T when a canopy was even a small fraction wet. After these modifications, in arid and semi-arid regions E_s and ET were reduced during wet periods leading to improved seasonality of ET and an increase in GPP. However, the impact of our modifications globally was for GPP to decrease slightly ($\sim$1.6%) compared to the baseline CLASSIC simulations as a result of increased T and ET and drier soils in other biomes including seasonally dry tropical forests. Globally, the proportion of T relative to ET was improved compared to observations with an increase from $\sim$25% in baseline CLASSIC to $\sim$41% in the DSL-EcT simulations. As the simulated global T/ET of 0.41 remains lower than observation-based estimates of 0.57 ± 0.07 (Wei et al., 2017), possible future improvements to CLASSIC include implementing terrain-driven lateral flow redistributing water, and including a plant hydraulics-based g_c scheme instead of an empirical moisture stress function to improve the representation of plant water use and the vegetation's response to drought stress. Improvements in ET partitioning in LSMs and ESMs are important to simulate carbon and water fluxes well in historical and especially future simulations, as warmer climates are expected to enhance water cycles and impact ESM climate simulations.

Appendix A

A1 Evapotranspiration parameterization

ET is the sum of E_s, E_c and T. E_s consists of E originating from bare soil and from soil underneath the vegetation canopy. The potential evaporation rate from bare soil, $E(0)$ (mm s^{-1}), is calculated as

$$E(0) = \rho_a C_{DH} v_a (q(0) - q_a), \tag{A1}$$

where ρ_a is the air density (kg m^{-3}), C_{DH} the stability-dependent surface drag coefficient for heat (unitless), v_a the wind speed at the reference height (m s^{-1}), $q(0)$ the specific humidity at the surface (kg kg^{-1}) and q_a the specific humidity at the reference height (kg kg^{-1}) (Verseghy, 2017). The saturated surface specific humidity, $q(0)_{sat}$ (kg kg^{-1}), q_a, and the surface evaporation efficiency (β; unitless; Equation A20) are used to determine $q(0)$ as

$$q(0) = \beta q(0)_{sat} + (1 - \beta) q_a. \tag{A2}$$

The surface evaporation rate is limited to a maximum value, $E(0)_{\max}$ (mm s^{-1}) determined by the water content of the top soil layer (θ_1; m^3 m^{-3}) and the depth of water ponded on the surface (Z_p, m) as

$$E(0)_{max} = \rho_w \left[Z_p + (\theta_1 - \theta_{min})\Delta Z_1\right]/\Delta t, \tag{A3}$$

with the density of water ρ_w (kg m^{-3}), the depth of the top soil layer ΔZ_1 (e.g. 0.10 m) and the time interval Δt (s) (typically 900-1800 s for CLASSIC) (Verseghy, 2017). θ_{min} (m^3 m^{-3}) is the residual soil liquid water content remaining after freezing or evaporation. This is set to 0.04 m^3 m^{-3} for mineral and fibric organic soils and 0.15 and 0.22 m^3 m^{-3} for hemic and sapric organic soils, respectively. Underneath the vegetation, the maximum surface evaporation rate, $E(0)_{\max,c}$ (mm s^{-1}), is determined as

$$E(0)_{max,c} = \rho_w (\theta_1 - \theta_{min})\Delta Z_1/\Delta t. \tag{A4}$$

The potential evaporation rate from soil under the vegetation, $E(0)_c$ (mm s^{-1}), is calculated as

$$E(0)_c = \frac{\rho_a}{r_{a,g}}(q(0) - q_{a,c}), \tag{A5}$$

where $q_{a,c}$ is the specific humidity of the canopy air (kg kg^{-1}) and $r_{a,g}$ (s m^{-1}) is the surface resistance, whose inverse is derived from Deardorff (1972) as

$$\frac{1}{r_{a,g}} = 1.9 \times 10^{-3}(T(0)_v - T_{ac,v})^{1/3}, \tag{A6}$$

with the virtual potential temperature at the surface ($T(0)_v$; K) and of the canopy air ($T_{ac,v}$; K) and the constant 1.9 × 10^{-3} in m s^{-1} K$^{-1/3}$. The evapotranspiration rate from the vegetation (ET$_c$; mm s^{-1}), i.e., the sum of E_c and T, which is equivalent to the latent heat flux from the vegetation canopy divided by the latent heat of vaporization, is calculated as

$$\mathrm{ET_c} = \rho_a \frac{q_c - q_{a,c}}{r_b + r_c}, \tag{A7}$$

where q_c is the saturated specific humidity at the canopy temperature (kg kg^{-1}), r_b the leaf boundary layer resistance (s m^{-1}) and r_c the stomatal resistance (s m^{-1}). The relative contributions from E or T differ depending on the circumstances in the model. If there is snow on the canopy, $\mathrm{ET_c}$ is limited to the intercepted snow amount and is in the form of E_c through sublimation. If instead, the canopy has liquid water upon it, the calculated $\mathrm{ET_c}$ is first drawn from the amount of liquid water stored on the canopy (W_l; kg m^{-2}). If that amount is insufficient to satisfy the calculated $\mathrm{ET_c}$, T is possible after checking there is enough soil water available in the root zone. E_c is then set to W_l and the remainder of $\mathrm{ET_c}$ is allocated to T. Thus, T only occurs, when there is no water available on the canopy and enough soil water is available, i.e., the liquid water content (θ_l; m^3 m^{-3}) exceeds θ_{min} for the respective soil layer. Based on Bonan (1996); McNaughton and Van Den Hurk (1995), the inverse of r_b is calculated as

$$1/r_b = v_{ac}^{1/2}\sigma f_i \gamma_i \mathrm{PAI}^{1/2}/0.75[1 - \exp(-0.75\mathrm{PAI}^{1/2})] \tag{A8}$$

with the wind speed in the canopy air space v_{ac}, the fractional coverage of each PFT f_i, the PFT-dependent parameter describing leaf dimension γ_i (unitless), and the plant area index (PAI). By default, CLASSIC uses Leuning (1995)'s stomatal conductance (g_c; mol CO_2 $m^{-2}s^{-1}$) formulation (details in Arora (2003); Melton and Arora (2016)) and g_c is calculated as

$$g_c = m\frac{G_{canopy,net}\ p}{(c_s - \Gamma)}\frac{1}{(1+\mathrm{VPD}/V_o)} + b\ \mathrm{LAI}, \tag{A9}$$

where $G_{canopy,net}$ is the net canopy photosynthesis rate (mol CO_2 m^{-2} s^{-1}), p is the surface atmospheric pressure (Pa) and Γ is the CO_2 compensation point (Pa). The parameter m (unitless) is 9.0 for needle-leaf trees, 12.0 for other C_3 plants and 6.0 for C_4 plants, b is set to 0.01 mol $m^{-2}s^{-1}$ for C_3 and 0.04 mol $m^{-2}s^{-1}$ for C_4 plants. The parameter V_o has values of 2000 Pa for trees and shrubs and 1500 Pa for crops and grasses. The partial pressure of CO_2 at the leaf surface, c_s (Pa), depends on the atmospheric CO_2 partial pressure c_{ap} (Pa), $G_{canopy,net}$ and the aerodynamic conductance g_b (mol CO_2 m^{-2} s^{-1}) and is defined as

$$c_s = c_{ap} - \frac{1.37\ G_{canopy,net}\ p}{g_b}. \tag{A10}$$

The units of g_c and g_b can be converted from mol CO_2 m^{-2} s^{-1} to m s^{-1} using

$$g_c(\mathrm{m\ s^{-1}}) = 0.0224\frac{T_c}{T_f}\frac{p_0}{p}g_c(\mathrm{mol\ CO_2\ m^{-2}\ s^{-1}}), \tag{A11}$$

with the standard atmospheric pressure p_0 = 101 325 Pa and the freezing temperature T_f = 273.16 K.

A2 Determination of the dry surface layer thickness

To avoid numerical instabilities due to thin soil layers, CLASSIC uses a 10 cm thick top soil layer. In reality, soil moisture can vary strongly within the top 10 cm of soil, especially during extended dry periods where a thin layer at the top of the soil surface gets very dry while the soil below stays moist (Goss & Madliger, 2007; Kurc & Small, 2004; Li et al., 2020). To approximate the effects of this thin dry layer on surface water and energy fluxes, a DSL parameterization is implemented in CLASSIC following Swenson and Lawrence (2014). Their DSL parameterization determines when a DSL is present, its thickness, and the resulting surface resistance to evaporation. The formation of a DSL is initiated when the soil moisture of the top soil layer falls below a defined moisture threshold, θ_{DSL0} (m^3 m^{-3}), which is determined as

$$\theta_{DSL0} = K\theta_{p,1}, \tag{A12}$$

where $\theta_{p,1}$ is the porosity of the top soil layer (m^3 m^{-3}) and K is a constant (unitless), here with a value of 0.8 following Swenson and Lawrence (2014). The thickness of the DSL (m) is calculated as

$$DSL = \begin{cases} z_{max}\frac{\theta_{DSL0}-(\theta_{l,1}+\theta_{ice,1})}{\theta_{DSL0}-\theta_{air}} & \text{for } \theta_{l,1}+\theta_{ice,1} < \theta_{DSL0} \\ 0 & \text{for } \theta_{l,1}+\theta_{ice,1} \geq \theta_{DSL0}, \end{cases} \tag{A13}$$

where z_{max} is the maximum DSL thickness (m), here set to 0.015 m. As the liquid (θ_l) and frozen (θ_{ice}) water contents of the bare ground and ground under canopy subareas can differ in CLASSIC, the DSL thickness and the resistance to evaporation are calculated separately for these two subareas. The “air-dry” soil moisture value (θ_{air}) was determined following Dingman (2002) as

$$\theta_{air} = \theta_{p,1} \left(\frac{\Psi_{sat,1}}{\Psi_{air}} \right)^{\frac{1}{b}} \tag{A14}$$

with the saturated soil matric potential Ψ_{sat} (m), the air-dry matric potential $\Psi_{air} = 10^4$ m (Swenson & Lawrence, 2014) and the Clapp and Hornberger empirical soil water characteristic “b” parameter (unitless). The soil resistance to evaporation from bare ground or the ground under the canopy R_{soil} (s m^{-1}) is determined as

$$R_{soil} = \frac{DSL}{\tau D_v}, \tag{A15}$$

where D_v (m^2 s^{-1}) is the molecular diffusivity of water vapour in the air and calculated as (D. M. Lawrence et al., 2020)

$$D_v = 2.12 \times 10^{-5} \left(\frac{T_1}{273.15} \right)^{1.75}, \tag{A16}$$

where T_1 is the temperature of the top soil layer (K). τ (m^3 m^{-3}) in Equation A15 is the tortuosity of the vapour flow paths through the soil and determined following Moldrup et al. (2003) as

$$\tau = \Phi_{air}^2 \left(\frac{\Phi_{air}}{\theta_{p,1}} \right)^{3/b} \tag{A17}$$

with the air-filled pore space Φ_{air} (m^3 m^{-3}) calculated as

$$\Phi_{air} = \theta_{p,1} - \theta_{air}. \tag{A18}$$

A3 DSL effect on surface evaporation

An increasing thickness of the DSL acts to decrease surface evaporation and thus the latent heat flux in CLASSIC through a decrease in the surface evaporation efficiency (β; unitless). β has a value between 0 and 1, where a value of 1 means that the specific humidity at the surface equals the saturated surface specific humidity and does not limit E, i.e. a DSL thickness of 0, whereas a β value of 0 means no surface evaporation can occur. β is calculated as the minimum, more limiting value, between the soil evaporation efficiency (R_{soil}; Equation A15) derived from the DSL thickness and that calculated by using CLASSIC's original soil evaporation efficiency (Meyer et al., 2021; Merlin et al., 2011) (CEVAP), which limits β values below 1 except when soils are fully saturated when the value can be 1.

$$\beta = \min \left(\frac{1}{C_{DH} v_a R_{soil} + 1}, \mathrm{CEVAP} \right). \tag{A19}$$

CEVAP is defined as

$$\mathrm{CEVAP} = \begin{cases} 0 & \text{for } \theta_{l,1} < \theta_{min} \\ 0.25(1 - \cos(\pi \theta_{l,1}/\theta_{p,1}))^2 & \text{for } \theta_{min} < \theta_{l,1} \leq \theta_{p,1}. \end{cases} \tag{A20}$$

When there is snow or ponded water on the surface, β is set to 1 and $q(0)$ is set to $q(0)_{sat}$. Equation A19 gives a β that is constrained to CEVAP, when the soil is too moist for a DSL to develop. Figure 1 shows an example of the soil evaporation efficiency determined using the original CEVAP parameterization as well as the calculation using the resistance due to the DSL and the minimum of the two parameterizations for a range of liquid water content values of the top soil layer.

571 **A4 DSL effect on the thermal conductivity**

In CLASSIC, the soil thermal conductivity (λ_{soil}; W m^{-1} K^{-1}) is determined from the saturated thermal conductivity (λ_{sat}; W m^{-1} K^{-1}), the dry thermal conductivity (λ_{dry}; W m^{-1} K^{-1}) and a relative thermal conductivity (λ_r; unitless; ranging from 0 for dry soils to 1 for saturated soils) following Côté and Konrad (2005) (Verseghy, 2017)

$$\lambda_{soil} = \lambda_r(\lambda_{sat} - \lambda_{dry}) + \lambda_{dry}. \tag{A21}$$

An empirical coefficient κ (unitless), which differs for frozen (κ = 1.2, 0.85, and 0.25 for coarse mineral, fine mineral, and organic soils, respectively) and unfrozen (κ = 4.0, 1.9, and 0.6 for coarse mineral, fine mineral, and organic soils, respectively) soils, and the degree of saturation (S_r; unitless) determine λ_r

$$\lambda_r = \frac{\kappa S_r}{1 + S_r(\kappa - 1)}, \tag{A22}$$

where

$$S_r = \frac{\theta_{l+ice}}{\theta_p}. \tag{A23}$$

λ_{dry} depends on θ_p and is calculated as

$$\lambda_{dry} = \begin{cases} 0.75\ exp(-2.76\ \theta_p) & \text{for mineral soil} \\ 0.30\ exp(-2.00\ \theta_p) & \text{for organic soil.} \end{cases} \tag{A24}$$

The thermal conductivities of liquid water (λ_l = 0.57 W m^{-1} K^{-1}), ice (λ_{ice} = 2.24 W m^{-1} K^{-1}) and the soil particles (λ_s; W m^{-1} K^{-1}; values are 2.5 W m^{-1} K^{-1} for sand and clay and 0.25 W m^{-1} K^{-1} for organic matter) determine λ_{sat} following De Vries (1963) as

$$\lambda_{sat} = \begin{cases} \lambda_l\theta_p + \lambda_s(1 - \theta_p) & \text{for unfrozen soil} \\ \lambda_{ice}\theta_p + \lambda_s(1 - \theta_p) & \text{for frozen soil.} \end{cases} \tag{A25}$$

Similar to the latent heat flux (Section A3), the sensible heat flux should be limited by the DSL because the thermal properties, i.e., the thermal conductivity and heat capacity, which is influenced by changes in soil moisture, of the DSL differ from those of the top soil layer, as the DSL is drier and has more air filled-pore space. When a DSL is present, for mineral soils and organic soils in uplands, the thermal conductivity at the top of the first soil layer (λ; W m^{-1} K^{-1}) is linearly interpolated between the "dry" (λ_{dry}) and calculated top soil layer thermal conductivity (λ_{soil}) values depending on the DSL thickness

$$\lambda = \lambda_{soil} - \frac{DSL}{z_{max}}(\lambda_{soil} - \lambda_{dry}). \tag{A26}$$

572 **A5 DSL effect on the ground albedo**

In CLASSIC, the visible and near-infrared ground albedos (α_g; unitless) are soil moisture dependent. As the top of the soil wets from a liquid water content value of 0.22 to 0.26 m^3 m^{-3}, the albedo values follow a linear relationship between the "dry" ($\alpha_{g,dry}$; unitless) and "wet" albedo values ($\alpha_{g,wet}$; unitless) of the respective soil colour index (P. J. Lawrence & Chase, 2007). Outside of this range of liquid water content, the model adopts either the dry or wet albedo value accordingly. With the DSL formulation, if a DSL exists, a DSL-dependent α_g is calculated as

$$\alpha_g = \alpha_{g,wet} - \frac{DSL}{z_{max}}(\alpha_{g,wet} - \alpha_{g,dry}) \tag{A27}$$

and the α_g value used by the model is set to the higher value of the original CLASSIC calculation and the value determined in Equation A27.

A6 Modifications to canopy evaporation and transpiration in CLASSIC

In the CLASSIC v.1.2 formulation for snow-covered canopies the evaporative flux from the canopy ($\mathrm{ET_c}$; Equation A7) is first assigned to sublimation, as liquid water, if present, is assumed to be within or underneath the snow and no T is expected to occur. When there is only liquid water present on the canopy, we modified the original formulation so that T is allowed to occur from a partially-wet canopy instead of from a completely dry canopy only. To separate the calculated amount of evapotranspired water ($\mathrm{ET_c}$; see Equation A7) into E_c and T, we determine the wet (f_{wet}) and dry (f_{dry}) fractions of the canopy similar to Fan et al. (2019) as

$$f_{wet} = \begin{cases} F_l & \text{for } F_l \geq 0.01 \text{ and } F_l \leq 0.99 \\ 0 & \text{for } F_l < 0.01 \\ 1 & \text{for } F_l > 0.99 \end{cases} \tag{A28}$$

$$f_{dry} = \begin{cases} (1 - f_{wet})\frac{\mathrm{LAI}}{\mathrm{PAI}} & \text{for } f_{wet} \geq 0.01 \text{ and } f_{wet} \leq 0.99 \\ 1 & \text{for } f_{wet} < 0.01 \\ 0 & \text{for } f_{wet} > 0.99 \end{cases} \tag{A29}$$

In general, only the leaves and not stems of a canopy can transpire, f_{dry} is adjusted by the LAI to PAI ratio. F_l is the fractional coverage of the canopy covered by liquid water (unitless) determined as

$$F_l = \begin{cases} \min(W_l \ / \ W_{l,max}, 1) & \text{for } W_{l,max} > 0) \\ 0 & \text{for } W_{l,max} = 0) \end{cases} \tag{A30}$$

where W_l (kg m^{-2}) is the amount of liquid water stored on the canopy and $W_{l,max}$ (kg m^{-2}) is the storage capacity of the canopy for liquid water, which is calculated as

$$W_{l,max} = p_l \times \mathrm{PAI} \tag{A31}$$

with the maximum storage of liquid water p_l set as 0.20 kg m^{-2} (Bartlett et al., 2006). W_l is calculated as the sum of W_l of the previous time step and the rainfall intercepted by the canopy during the current time step

$$W_{l,t} = \min(W_{l,t-1} + \Delta t \rho_w (P - \chi P), W_{l,max}), \tag{A32}$$

where P is the rainfall rate (m s^{-1}), χ is the canopy gap fraction (unitless), Δt is the model physics timestep (s) and ρ_w (kg m^{-3}) the density of liquid water. To determine the canopy fractional coverage of liquid water exposed to the air, F_l is decreased by the fractional snow coverage (F_s).

$$F_l = \max(0, \min(F_l - F_s, 1)) \tag{A33}$$

and, similar to F_l, F_s is found by

$$F_s = \begin{cases} \min(W_f \ / \ W_{f,max}, 1) & \text{for } W_{f,max} > 0) \\ 0 & \text{for } W_{f,max} = 0), \end{cases} \tag{A34}$$

where W_f (kg m^{-2}) is the amount of frozen water stored on the canopy and $W_{f,max}$ (kg m^{-2}) is the storage capacity of the canopy for frozen water. If there is no plant available water in the root zone, the wet canopy fraction is set to 1, as T is not allowed to occur.

The predicted mass of water evapotranspired from the canopy (W_E; kg m^{-2}) is calculated as

$$W_E = \mathrm{ET_c} \times \rho_w \Delta t, \tag{A35}$$

where $\mathrm{ET_c}$ is the evapotranspiration rate from the canopy (m s^{-1}; see Equation A7). The wet and dry canopy fractions as well as F_{RbRc} determine the fractions of W_E coming from

E_c and T, respectively. The amount of W_l (see Equation A32) is adjusted by the amount of water evaporated from the wet canopy fraction as

$$W_l = W_l \text{ - } (1 \text{ - } f_{dry})\ (1 \text{ - } F_{RbRc})\ W_E \text{ for } W_E\ (1 \text{ - } f_{dry})(1 \text{ - } F_{RbRc}) \leq W_l \tag{A36}$$

and W_E is reduced by the amount being evaporated

$$W_E = \begin{cases} W_E\ (F_{RbRc} + f_{dry} \text{ - } f_{dry}\ F_{RbRc}) & \text{for } W_E\ (1 \text{ - } f_{dry})\ (1 \text{ - } F_{RbRc}) \leq W_l \\ W_E \text{ - } W_l & \text{for } W_E\ (1 \text{ - } f_{dry})\ (1 \text{ - } F_{RbRc}) > W_l \end{cases} \tag{A37}$$

The contribution of the leaf boundary layer resistance (r_b; s m^{-1}; Equation A8) to the total resistance, the sum of r_b and the stomatal resistance (r_c or $1/g_c$; s m^{-1}; Equation A9), is calculated as a proportion of the total resistance from the leaf boundary layer and stomata to determine when canopy evaporation is dominant and when T can occur, as

$$F_{RbRc} = r_b/(r_b + r_c). \tag{A38}$$

In the second case of Equation A37, where W_l could not meet the calculated amount of water to be evaporated, W_l is then set to zero. If the predicted mass of water evapotranspired from the vegetation (W_E) after considering evaporation from wet leaves is greater than zero, it is treated as T. If there is enough water available in the root zone and T can occur, the soil water content removed by T and the T flux are calculated for each soil layer and the liquid water content of each soil layer containing roots is updated.

Appendix B

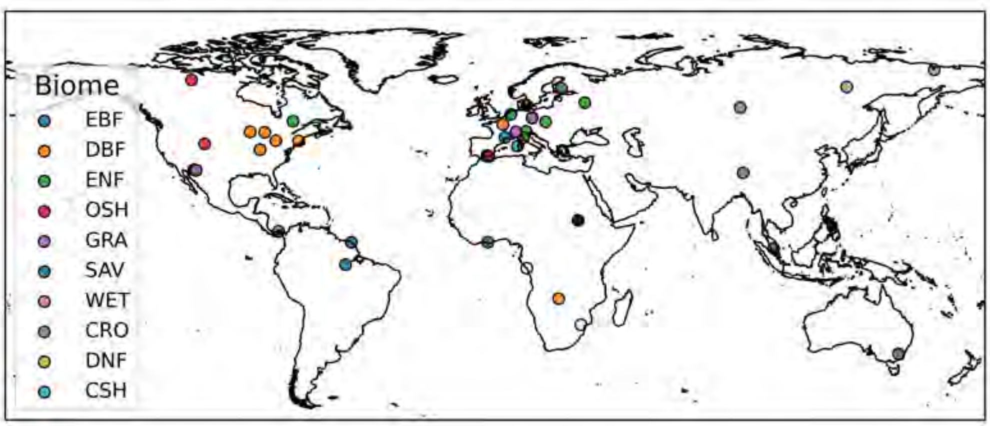

Figure B1: Map of the FLUXNET sites used in this study (including their biomes).

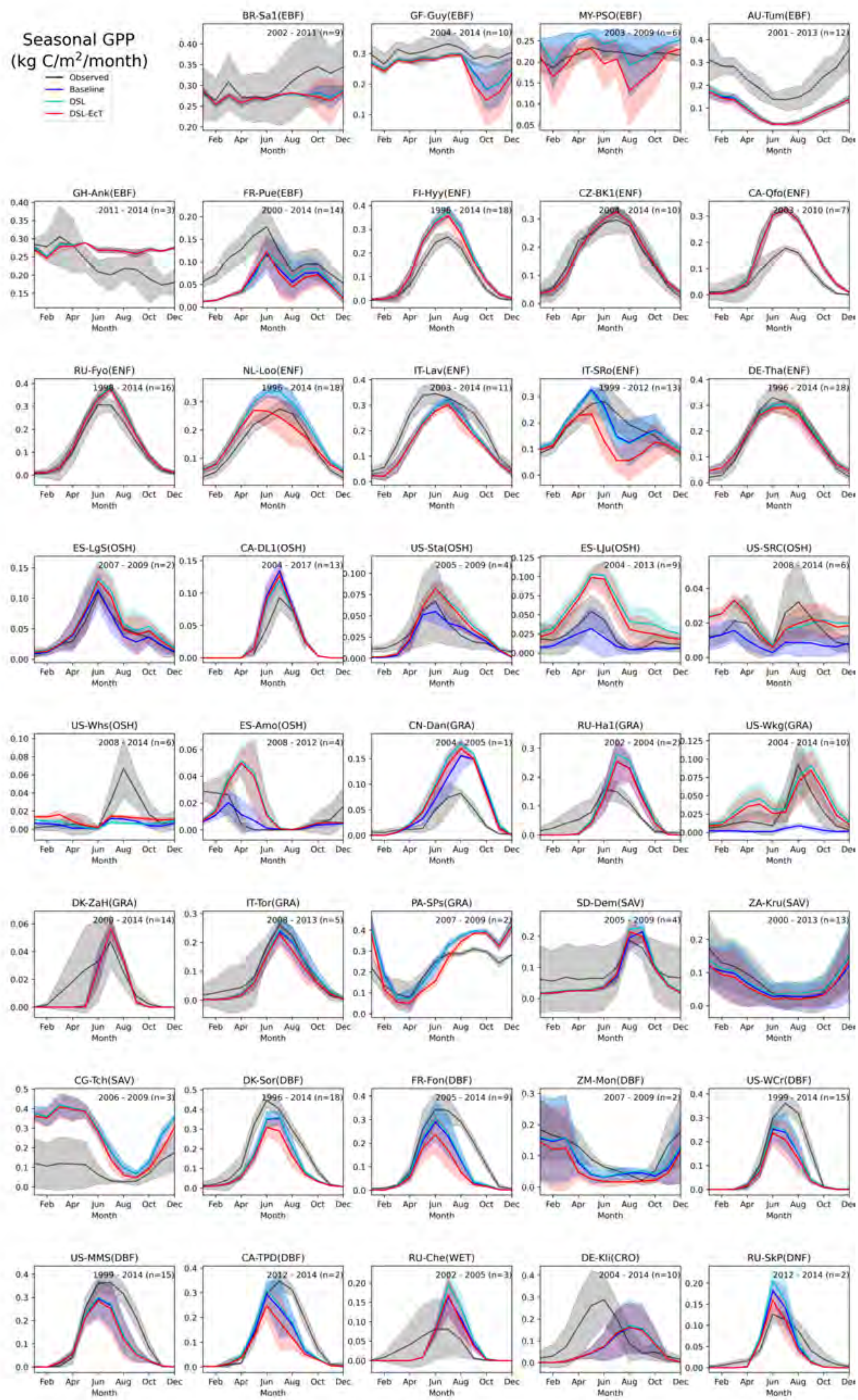

Figure B2: Monthly mean observed and simulated gross primary productivity (GPP) for the FLUXNET sites for the Baseline, DSL and DSL-EcT simulations (Table 1). The shading shows the standard deviation over the available years. Site names, their biomes and years of measurements used are listed for each site in Table 2.

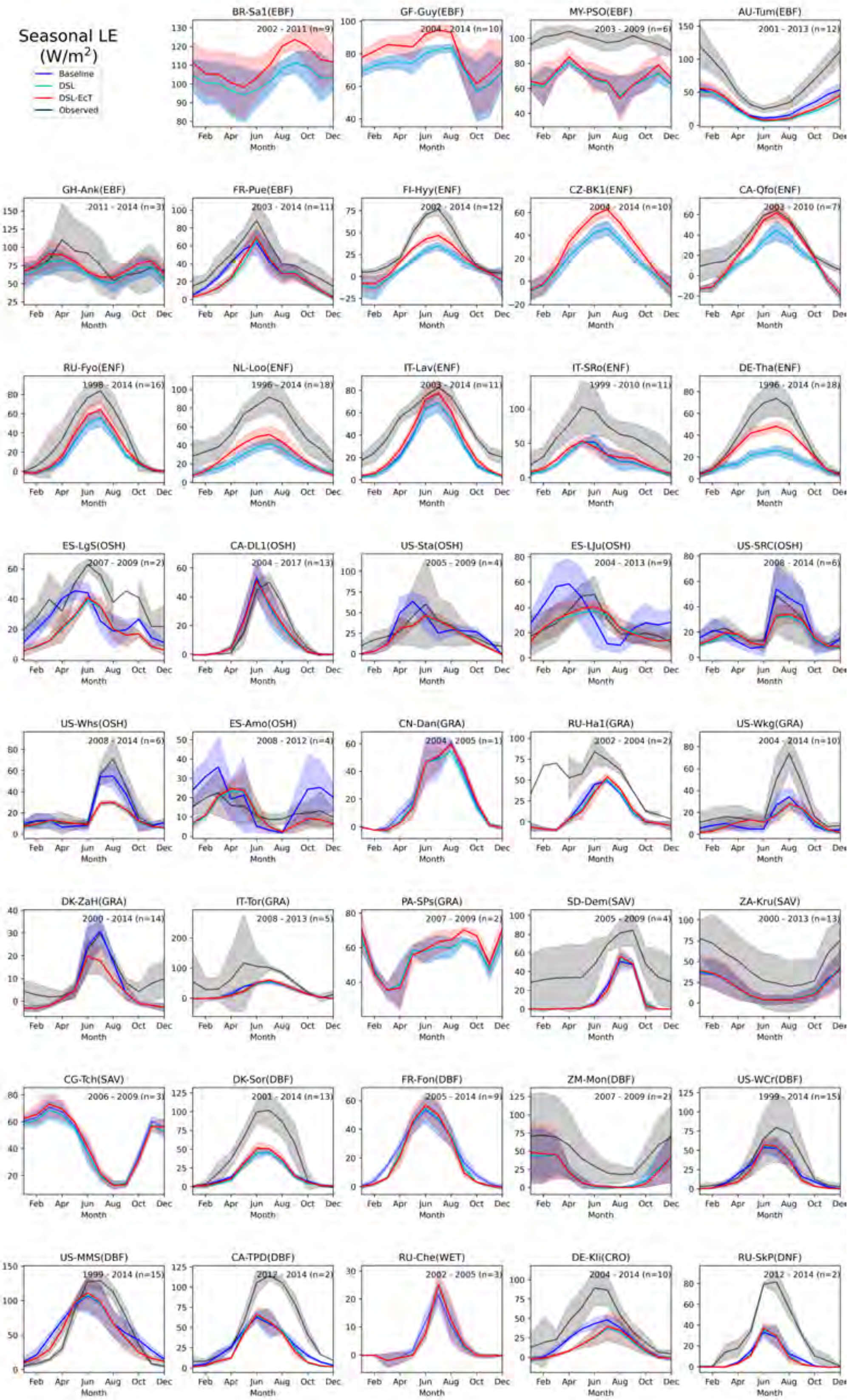

Figure B3: Monthly mean observed and simulated latent heat flux (LE) for the FLUXNET sites for the Baseline, DSL and DSL-EcT simulations (Table 1).

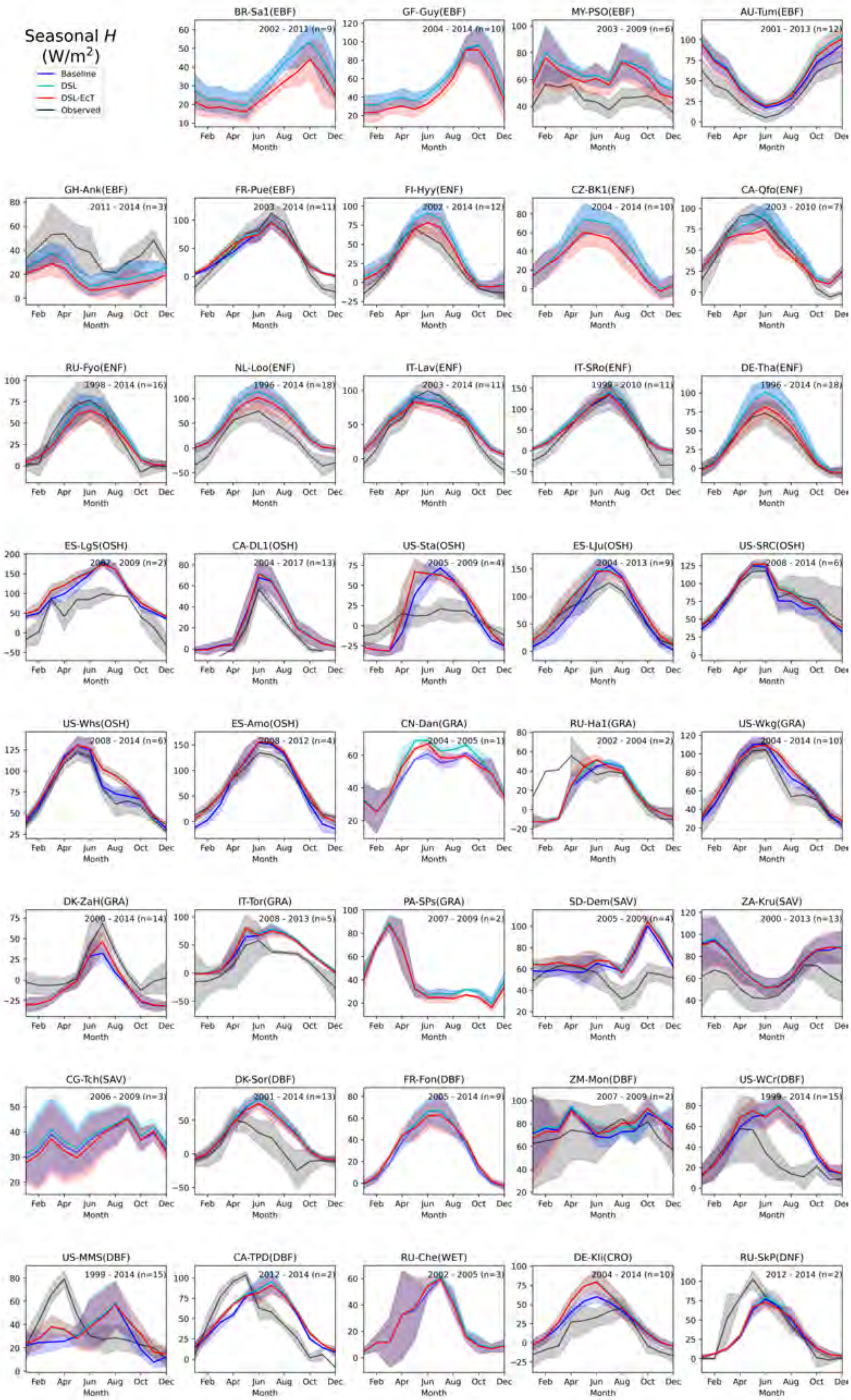

Figure B4: Monthly mean observed and simulated sensible heat flux (H) for the FLUXNET sites for the Baseline, DSL and DSL-EcT simulations (Table 1).

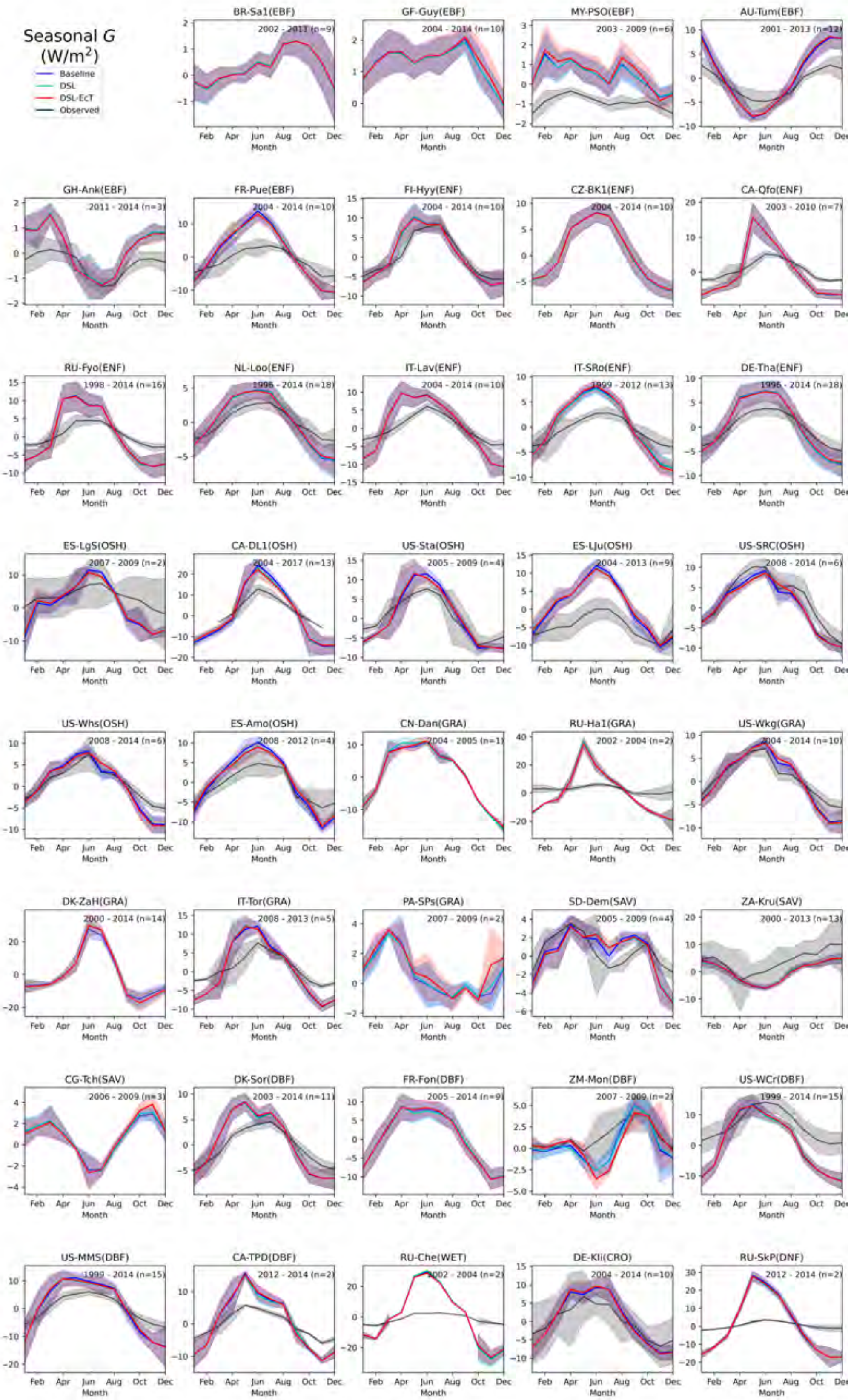

Figure B5: Monthly mean observed and simulated ground heat flux (G) for the FLUXNET sites for the Baseline, DSL and DSL-EcT simulations (Table 1).

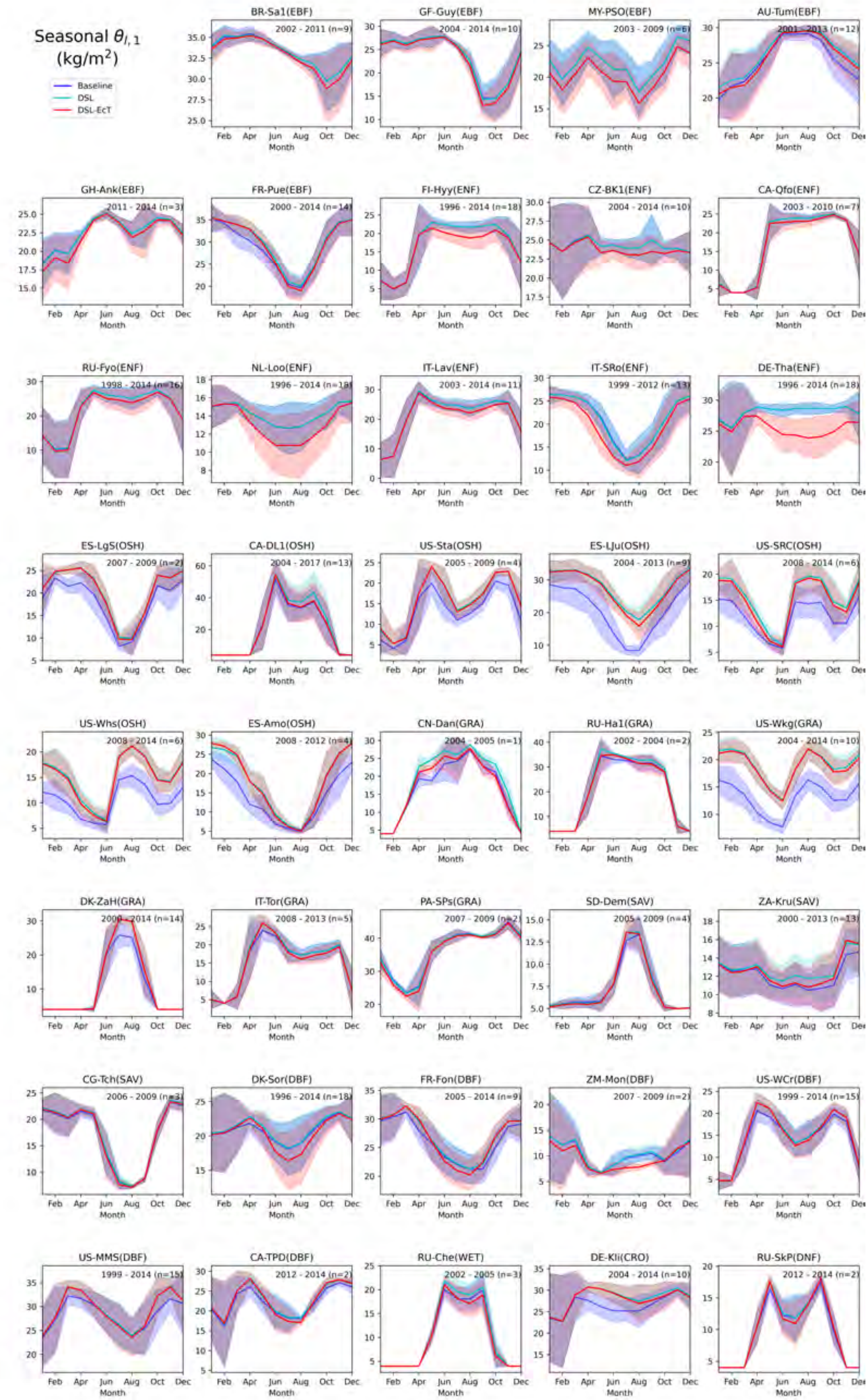

Figure B6: Monthly mean simulated liquid water content of the top soil layer (0-10 cm depth; $\theta_{l,1}$) for the FLUXNET sites for the Baseline, DSL and DSL-EcT simulations (Table 1).

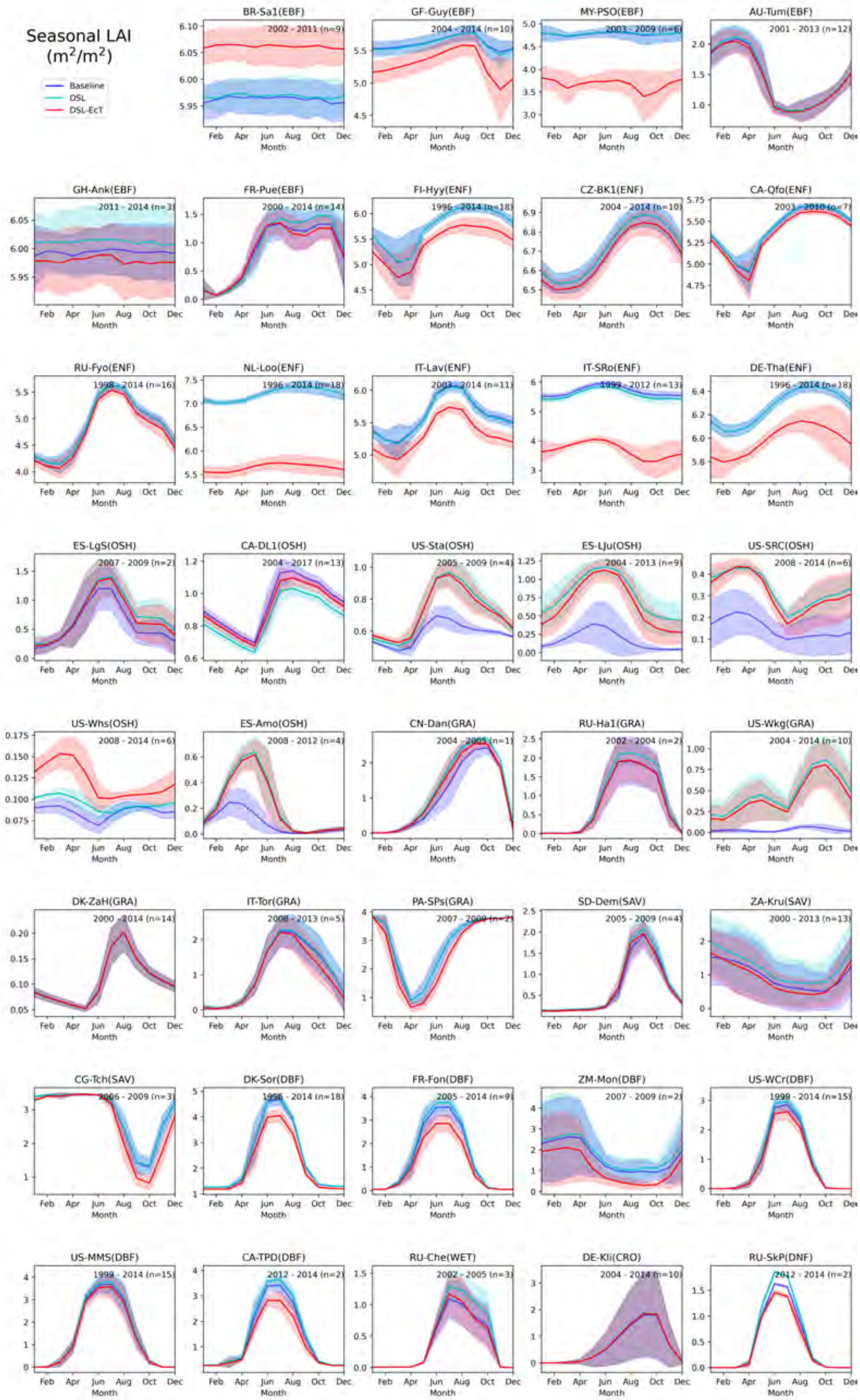

Figure B7: Monthly mean simulated leaf area index (LAI) for the FLUXNET sites for the Baseline, DSL and DSL-EcT simulations (Table 1).

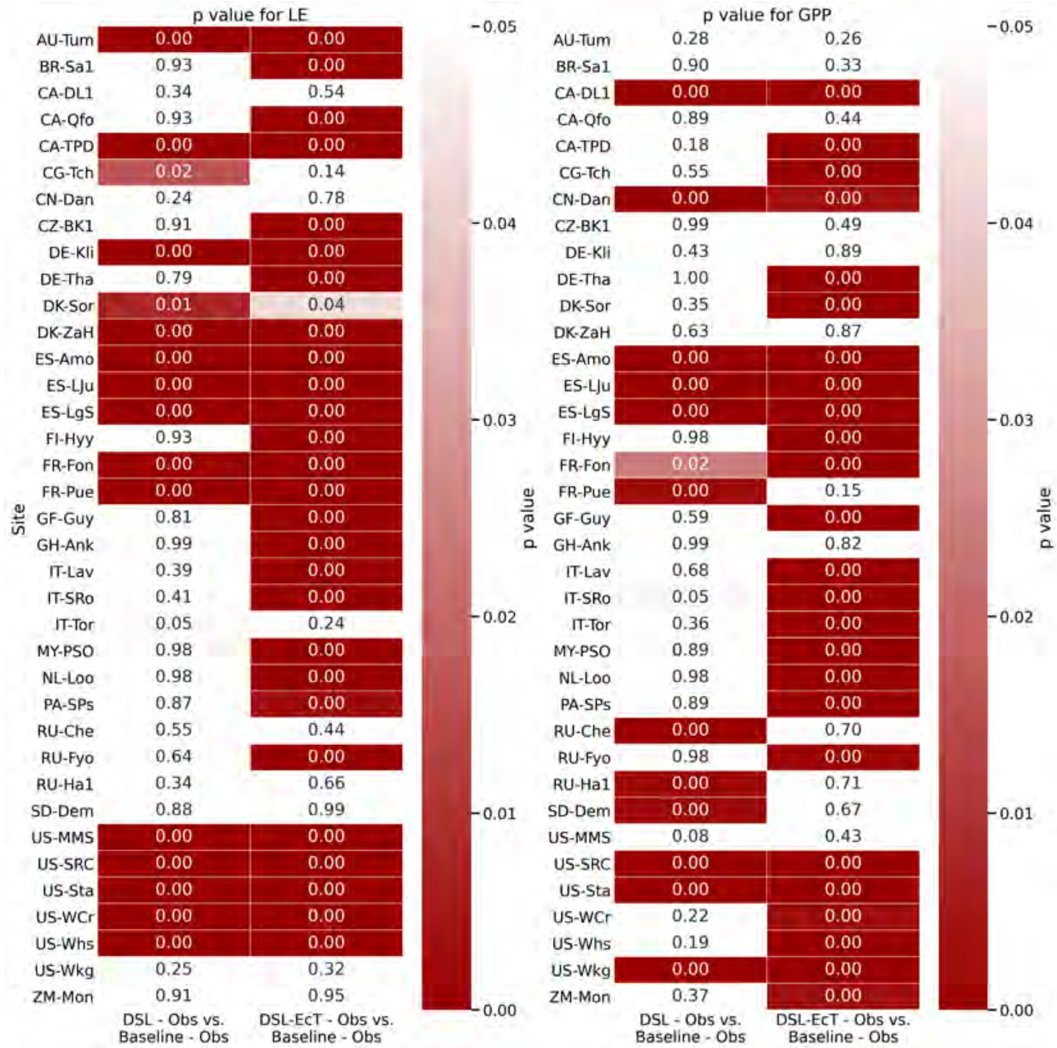

Figure B8: Two-sided t-test p value between the error in simulated daily gross primary productivity (GPP) and latent heat flux (LE) for the FLUXNET sites (Table 2) for DSL and DSL-EcT simulations compared to the Baseline simulation (Table 1).

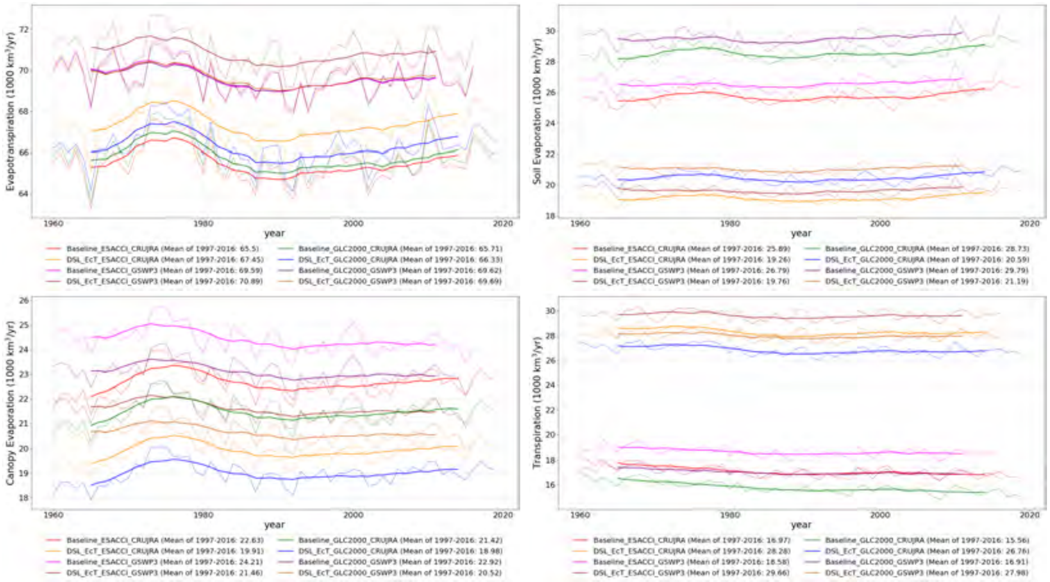

Figure B9: Annual ET, soil E, canopy E and T for 1960-2016 for the four Baseline and DSL-EcT simulations (Table 1), respectively.

Table B1: Transpiration (T) to evapotranspiration (ET) ratios of the different CLASSIC simulations (Table 1) averaged over 1997-2016.

Forcing data	**Baseline**	**DSL**	**DSL-EcT**
ESACCI and CRUJRA	25.92%	30.33%	41.93%
ESACCI and GSWP3	26.72%	31.43%	41.85%
GLC2000 and CRUJRA	23.69%	28.62%	40.35%
GLC2000 and GSWP3	24.30%	29.48%	40.17%

Appendix C

Zonal ensemble plots of Baseline and DSL-EcT simulations show slight differences in GPP with the DSL-EcT simulations having slightly lower GPP in the Tropics and slightly higher GPP in the higher latitudes than the Baseline simulations. Globally, GPP is lower in the DSL-EcT simulations and shows less variability between the four simulations (using two different meteorological forcings and two different land cover representations) (Figure C1). In the Tropics, LE tends to be higher in the DSL-EcT simulations.

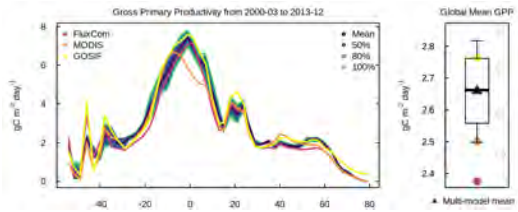

(a) Baseline

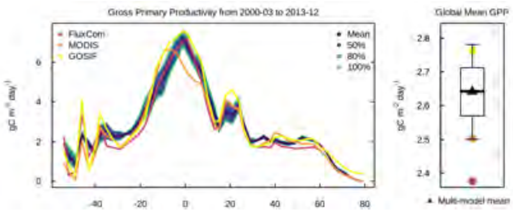

(b) DSL-EcT

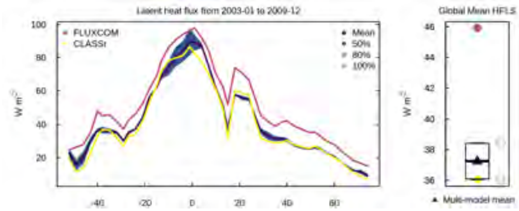

(c) Baseline

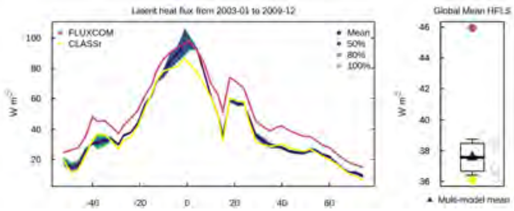

(d) DSL-EcT

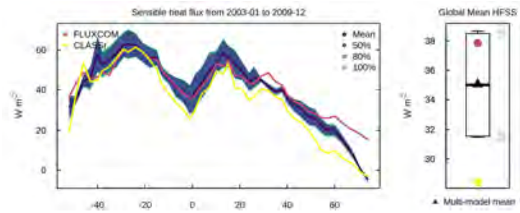

(e) Baseline

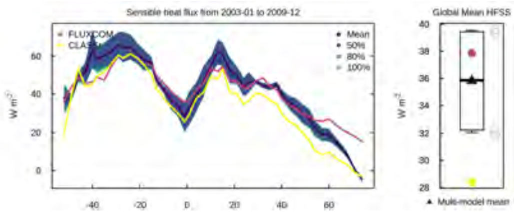

(f) DSL-EcT

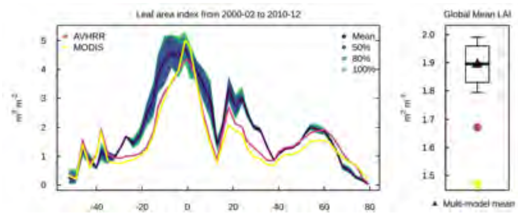

(g) Baseline

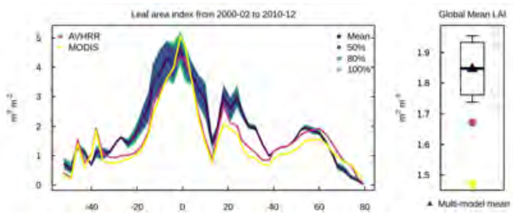

(h) DSL-EcT

Figure C1: Zonally averaged and global mean GPP, LE, H and LAI over land for the Baseline and DSL-EcT simulations. The ensemble includes the four simulations using a combination of two different meteorological forcing datasets and two land cover representations (Table 1).

593 Seasonal averages for the 11 TRANSCOM regions show that the Baseline and DSL
594 simulations have the greatest differences in the North American Boreal, the South Amer-
595 ican Tropics, Eurasian Temperate and Australia. During the spring, the DSL simula-
596 tions tend to overestimate GPP in Australia (Figure C2), while they perform well dur-
597 ing the rest of the year.

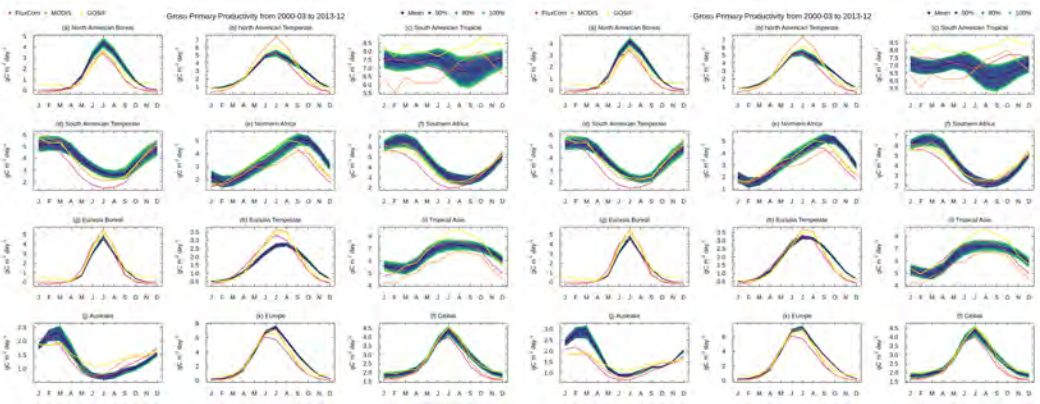

(a) Baseline (b) DSL-EcT

Figure C2: Monthly averaged GPP for 11 TRANSCOM regions and globally from March 2000 to December 2013.

In LE and H (Figure C3 and C4), the Baseline and DSL simulations show differences especially in the South American Tropical, Northern Africa and Tropical Asia. However, in all of the TRANSCOM regions as well as globally both simulations tend to lie within the uncertainty bounds of observations.

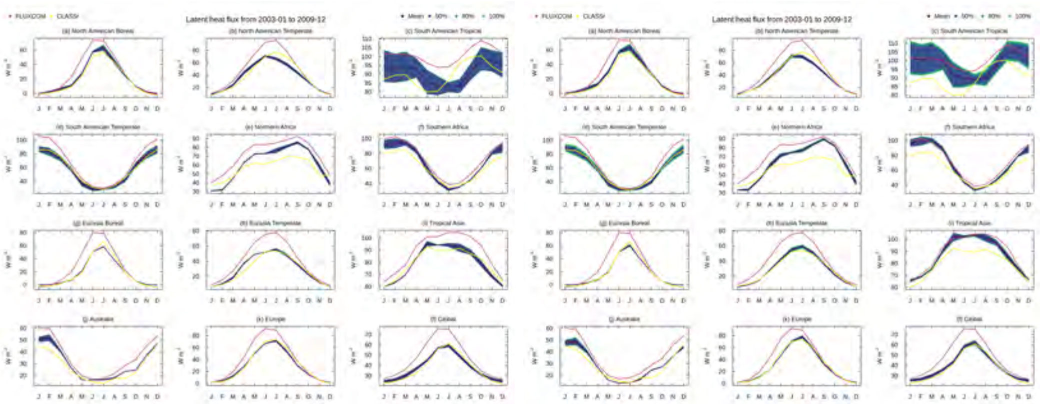

(a) Baseline (b) DSL-EcT

Figure C3: Monthly averaged LE for 11 TRANSCOM regions and globally from January 2003 to December 2009.

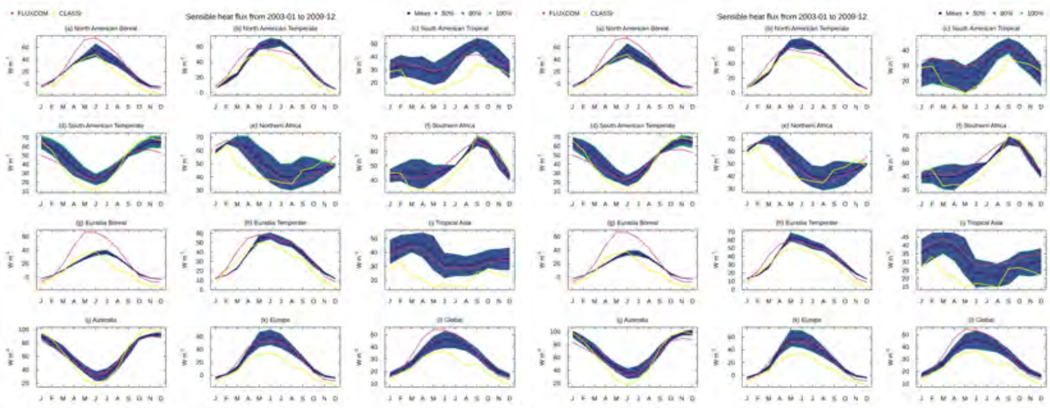

(a) Baseline (b) DSL-EcT

Figure C4: Monthly averaged H for 11 TRANSCOM regions and globally from January 2003 to December 2009.

Appendix D Open Research

D1 Data Availability Statement

The CLASSIC code versions (Baseline, DSL and DSL-EcT) and model outputs presented in our paper are archived on Zenodo (https://doi.org/10.5281/zenodo.7015764; Meyer et al. (2022)).

Acknowledgments

This work used eddy covariance data acquired and shared by the FLUXNET community, including these networks: AmeriFlux, AfriFlux, AsiaFlux, CarboAfrica, CarboEuropeIP, CarboItaly, CarboMont, ChinaFlux, Fluxnet-Canada, GreenGrass, ICOS, KoFlux, LBA, NECC, OzFlux-TERN, TCOS-Siberia, and USCCC. The FLUXNET eddy covariance data processing and harmonization were carried out by the European Fluxes Database Cluster, AmeriFlux Management Project, and Fluxdata project of FLUXNET with the support of CDIAC and ICOS Ecosystem Thematic Center, and the OzFlux, ChinaFlux, and AsiaFlux offices. We thank Christian Seiler for providing comments on a pre-submission version of the manuscript.

References

Arora, V. K. (2003, August). Simulating energy and carbon fluxes over winter wheat using coupled land surface and terrestrial ecosystem models. *Agric. For. Meteorol.*, *118*(1), 21–47. doi: 10.1016/S0168-1923(03)00073-X

Baldocchi, D., Falge, E., Gu, L., Olson, R., Hollinger, D., Running, S., … Wofsy, S. (2001, November). FLUXNET: A new tool to study the temporal and spatial variability of Ecosystem-Scale carbon dioxide, water vapor, and energy flux densities. *Bull. Am. Meteorol. Soc.*, *82*(11), 2415–2434. doi: 10.1175/1520-0477(2001)082⟨2415:FANTTS⟩2.3.CO;2

Barr, A. G., King, K. M., Gillespie, T. J., Den Hartog, G., & Neumann, H. H. (1994, October). A comparison of bowen ratio and eddy correlation sensible and latent heat flux measurements above deciduous forest. *Bound.-Layer Meteorol.*, *71*(1), 21–41. doi: 10.1007/BF00709218

Bartlett, P. A., MacKay, M. D., & Verseghy, D. L. (2006, September). Modified snow algorithms in the canadian land surface scheme: Model runs and sensitivity analysis at three boreal forest stands. *Atmosphere-Ocean*, *44*(3), 207–222. doi: 10.3137/ao.440301

Bonan, G. B. (1996). A land surface model (LSM version 1.0) for ecological, hydrological and atmospheric studies: Technical description and user's guide. NCAR technical note No. NCAR/TN-417+STR. *National Center for Atmospheric Research, Boulder, CO*, *150*. doi: 10.5065/D6DF6P5X

Čermák, J., Kučera, J., & Nadezhdina, N. (2004, September). Sap flow measurements with some thermodynamic methods, flow integration within trees and scaling up from sample trees to entire forest stands. *Trees*, *18*(5), 529–546. doi: 10.1007/s00468-004-0339-6

Chang, L., Dwivedi, R., Knowles, J. F., Fang, Y., Niu, G., Pelletier, J. D., ... Meixner, T. (2018, Sep 16,). Why Do Large-Scale Land Surface Models Produce a Low Ratio of Transpiration to Evapotranspiration? *Journal of Geophysical Research: Atmospheres*, *123*(17), 9109-9130. Retrieved from https://onlinelibrary.wiley.com/doi/abs/10.1029/2018JD029159 doi: 10.1029/2018JD029159

Chen, L., Sela, S., Svoray, T., & Assouline, S. (2013, September). The role of soil-surface sealing, microtopography, and vegetation patches in rainfall-runoff processes in semiarid areas. *Water Resour. Res.*, *49*(9), 5585–5599. doi: 10.1002/wrcr.20360

Coenders-Gerrits, A. M. J., van der Ent, R. J., Bogaard, T. A., Wang-Erlandsson, L., Hrachowitz, M., & Savenije, H. H. G. (2014, February). Uncertainties in transpiration estimates. *Nature*, *506*(7487), E1–2. doi: 10.1038/nature12925

Côté, J., & Konrad, J.-M. (2005, April). A generalized thermal conductivity model for soils and construction materials. *Can. Geotech. J.*, *42*(2), 443–458. doi: 10.1139/t04-106

CRU-JRA. (2021, July). *CRU-JRA v2.2: A forcings dataset of gridded land surface blend of climatic research unit (CRU) and japanese reanalysis (JRA) data; jan.1901 - dec.2020.*

Deardorff, J. W. (1972, February). Parameterization of the planetary boundary layer for use in general circulation models. *Mon. Weather Rev.*, *100*(2), 93–106. doi: 10.1175/1520-0493(1972)100⟨0093:POTPBL⟩2.3.CO;2

Decharme, B., Delire, C., Minvielle, M., Colin, J., Vergnes, J.-P., Alias, A., ... Voldoire, A. (2019, May). Recent changes in the ISBA-CTRIP land surface system for use in the CNRM-CM6 climate model and in global off-line hydrological applications. *J. Adv. Model. Earth Syst.*, *11*(5), 1207–1252. doi: 10.1029/2018ms001545

Decker, M., Or, D., Pitman, A., & Ukkola, A. (2017, jan). New turbulent resistance parameterization for soil evaporation based on a pore-scale model: Impact on surface fluxes in CABLE. *Journal of Advances in Modeling Earth Systems*, *9*(1), 220–238. Retrieved from https://doi.org/10.1002%2F2016ms000832 doi: 10.1002/2016ms000832

Dee, D. P., Uppala, S. M., Simmons, A. J., Berrisford, P., Poli, P., Kobayashi, S., ... Vitart, F. (2011, April). The ERA-Interim reanalysis: configuration and performance of the data assimilation system. *Quart. J. Roy. Meteor. Soc.*, *137*(656), 553–597. doi: 10.1002/qj.828

De Pue, J., Barrios, J. M., Liu, L., Ciais, P., Arboleda, A., Hamdi, R., ... Gellens-Meulenberghs, F. (2022). Local scale evaluation of the simulated interactions between energy, water and vegetation in land surface models. *Biogeosciences Discussions*, 1–44. Retrieved from https://bg.copernicus.org/preprints/bg-2021-355/ doi: 10.5194/bg-2021-355

De Vries, D. (1963). *Thermal properties of soils, in physics of plant environment, wrv wijk, editor.* North-Holland Pub. Co., Amsterdam.

Dingman, S. L. (2002). *Physical hydrology.* Prentice Hall.

Dirmeyer, P. A., Gao, X., Zhao, M., Guo, Z., Oki, T., & Hanasaki, N. (2006, October). GSWP-2: Multimodel analysis and implications for our perception of the land surface. *Bull. Am. Meteorol. Soc.*, *87*(10), 1381–1398. doi: 10.1175/BAMS-87-10-1381

Dong, J., Dirmeyer, P. A., Lei, F., Anderson, M. C., Holmes, T. R. H., Hain, C., & Crow, W. T. (2020, November). Soil evaporation stress determines soil Moisture-Evapotranspiration coupling strength in land surface modeling. *Geophys. Res. Lett.*, *47*(21), 12. doi: 10.1029/2020GL090391

Dong, J., Lei, F., & Crow, W. T. (2022, January). Land transpiration-evaporation partitioning errors responsible for modeled summertime warm bias in the central united states. *Nat. Commun.*, *13*(1), 336. doi: 10.1038/s41467-021-27938-6

Eller, C. B., Rowland, L., Oliveira, R. S., Bittencourt, P. R. L., Barros, F. V., da Costa, A. C. L., ... Cox, P. (2018, October). Modelling tropical forest responses to drought and el niño with a stomatal optimization model based on xylem hydraulics. *Philos. Trans. R. Soc. Lond. B Biol. Sci.*, *373*(1760). doi: 10.1098/rstb.2017.0315

ESA. (2017). *Land cover CCI product user guide version 2* (Vol. 2; Tech. Rep.). `maps.elie.ucl.ac.be/CCI/viewer/download/ESACCI-LC-Ph2-PUGv2_2.0.pdf`.

Fan, Y., Meijide, A., Lawrence, D. M., Roupsard, O., Carlson, K. M., Chen, H., ... Knohl, A. (2019, March). Reconciling canopy interception parameterization and rainfall forcing frequency in the community land model for simulating evapotranspiration of rainforests and oil palm plantations in indonesia. *J. Adv. Model. Earth Syst.*, *11*(3), 732–751. doi: 10.1029/2018MS001490

Fatichi, S., Or, D., Walko, R., Vereecken, H., Young, M. H., Ghezzehei, T. A., ... Avissar, R. (2020, January). Soil structure is an important omission in earth system models. *Nat. Commun.*, *11*(1), 522. doi: 10.1038/s41467-020-14411-z

Fisher, J. B., Tu, K. P., & Baldocchi, D. D. (2008, March). Global estimates of the land–atmosphere water flux based on monthly AVHRR and ISLSCP-II data, validated at 16 FLUXNET sites. *Remote Sens. Environ.*, *112*(3), 901–919. doi: 10.1016/j.rse.2007.06.025

Gash, J. H. C. (1979, January). An analytical model of rainfall interception by forests. *Quart. J. Roy. Meteor. Soc.*, *105*(443), 43–55. doi: 10.1002/qj.49710544304

Gavilán, P., & Berengena, J. (2007, January). Accuracy of the bowen ratio-energy balance method for measuring latent heat flux in a semiarid advective environment. *Irrig. Sci.*, *25*(2), 127–140. doi: 10.1007/s00271-006-0040-1

Good, S. P., Noone, D., & Bowen, G. (2015, July). WATER RESOURCES. hydrologic connectivity constrains partitioning of global terrestrial water fluxes. *Science*, *349*(6244), 175–177. doi: 10.1126/science.aaa5931

Goss, K.-U., & Madliger, M. (2007, May). Estimation of water transport based on in situ measurements of relative humidity and temperature in a dry tanzanian soil. *Water Resour. Res.*, *43*(5). doi: 10.1029/2006wr005197

Güntner, A. (2008, October). Improvement of global hydrological models using GRACE data. *Surv. Geophys.*, *29*(4), 375–397. doi: 10.1007/s10712-008-9038-y

Gupta, S., Lehmann, P., Bonetti, S., Papritz, A., & Or, D. (2021, April). Global prediction of soil saturated hydraulic conductivity using random forest in a covariate-based GeoTransfer function (CoGTF) framework. *J. Adv. Model. Earth Syst.*, *13*(4). doi: 10.1029/2020ms002242

Hadiwijaya, B., Isabelle, P.-E., Nadeau, D. F., & Pepin, S. (2021, February). Observations of canopy storage capacity and wet canopy evaporation in a humid boreal forest. *Hydrol. Process.*, *35*(2). doi: 10.1002/hyp.14021

Haghighi, E., & Or, D. (2015, June). Linking evaporative fluxes from bare soil across surface viscous sublayer with the Monin–Obukhov atmospheric flux-profile estimates. *J. Hydrol.*, *525*, 684–693. doi: 10.1016/j.jhydrol.2015.04.019

Harris, I., Jones, P. D., Osborn, T. J., & Lister, D. H. (2014, March). Updated high-resolution grids of monthly climatic observations - the CRU TS3.10 dataset. *Int. J. Climatol.*, *34*(3), 623–642. doi: 10.1002/joc.3711

Harris, I., Osborn, T. J., Jones, P., & Lister, D. (2020, April). Version 4 of the CRU TS monthly high-resolution gridded multivariate climate dataset. *Sci Data*, *7*(1), 109. doi: 10.1038/s41597-020-0453-3

Herbst, M., Rosier, P. T. W., McNeil, D. D., Harding, R. J., & Gowing, D. J. (2008, October). Seasonal variability of interception evaporation from the canopy of a mixed deciduous forest. *Agric. For. Meteorol.*, *148*(11), 1655–1667. doi: 10.1016/j.agrformet.2008.05.011

Jasechko, S., Sharp, Z. D., Gibson, J. J., Birks, S. J., Yi, Y., & Fawcett, P. J. (2013, April). Terrestrial water fluxes dominated by transpiration. *Nature*, *496*(7445), 347–350. doi: 10.1038/nature11983

Jung, M., Reichstein, M., & Bondeau, A. (2009, October). Towards global empirical upscaling of FLUXNET eddy covariance observations: validation of a model tree ensemble approach using a biosphere model. *Biogeosciences*, *6*(10), 2001–2013. doi: 10.5194/bg-6-2001-2009

Jung, M., Reichstein, M., Ciais, P., Seneviratne, S. I., Sheffield, J., Goulden, M. L., … Zhang, K. (2010, October). Recent decline in the global land evapotranspiration trend due to limited moisture supply. *Nature*, *467*(7318), 951–954. doi: 10.1038/nature09396

Kobayashi, S., Ota, Y., Harada, Y., Ebita, A., Moriya, M., Onoda, H., … Takahashi, K. (2015). The JRA-55 reanalysis: General specifications and basic characteristics. *Journal of the Meteorological Society of Japan. Ser. II*, *93*(1), 5–48. doi: 10.2151/jmsj.2015-001

Kurc, S. A., & Small, E. E. (2004, September). Dynamics of evapotranspiration in semiarid grassland and shrubland ecosystems during the summer monsoon season, central new mexico. *Water Resour. Res.*, *40*(9). doi: 10.1029/2004wr003068

Lange, S. (2020). *The Inter-Sectoral Impact Model Intercomparison Project Input data set: GSWP3-W5E5.* Retrieved from `https://www.isimip.org/gettingstarted/input-data-bias-correction/details/80/` (Accessed on July 29, 2020)

Lawrence, D. M., Fisher, R. A., Koven, C. D., Oleson, K. W., Swenson, S. C., Vertenstein, M., … Zeng, X. (2020, March). Technical description of version 5.0 of the community land model (CLM) [Computer software manual].

Lawrence, D. M., Oleson, K. W., Flanner, M. G., Thornton, P. E., Swenson, S. C., Lawrence, P. J., … Slater, A. G. (2011, January). Parameterization improvements and functional and structural advances in version 4 of the community land model. *J. Adv. Model. Earth Syst.*, *3*(1). doi: 10.1029/2011ms00045

Lawrence, P. J., & Chase, T. N. (2007, March). Representing a new MODIS consistent land surface in the community land model (CLM 3.0). *J. Geophys. Res.*, *112*(G1). doi: 10.1029/2006jg000168

Lee, T. J., & Pielke, R. A. (1992, May). Estimating the soil surface specific humidity. *J. Appl. Meteorol.*, *31*(5), 480–484. doi: 10.1175/1520-0450(1992)031⟨0480:ETSSSH⟩2.0.CO;2

Le Quéré, C., Andrew, R. M., Friedlingstein, P., Sitch, S., Hauck, J., Pongratz, J., … Zheng, B. (2018, dec). Global Carbon Budget 2018. *Earth System Science Data*, *10*(4), 2141–2194. Retrieved from `https://doi.org/10.5194%2Fessd-10-2141-2018` doi: 10.5194/essd-10-2141-2018

Leuning, R. (1995, April). A critical appraisal of a combined stomatal-photosynthesis model for C3 plants. *Plant Cell Environ.*, *18*(4), 339–355. doi: 10.1111/j.1365-3040.1995.tb00370.x

Li, Z., Vanderborght, J., & Smits, K. M. (2020, January). The effect of the top soil layer on moisture and evaporation dynamics. *Vadose Zone J.*, *19*(1). doi: 10.1002/vzj2.20049

Lian, X., Piao, S., Huntingford, C., Li, Y., Zeng, Z., Wang, X., ... Wang, T. (2018, Jul). Partitioning global land evapotranspiration using CMIP5 models constrained by observations. *Nature Climate Change*, *8*(7), 640-646. Retrieved from `https://search.proquest.com/docview/2061820602` doi: 10.1038/s41558-018-0207-9

MacBean, N., Scott, R. L., Biederman, J. A., Ottlé, C., Vuichard, N., Ducharne, A., ... Moore, D. J. P. (2020, November). Testing water fluxes and storage from two hydrology configurations within the ORCHIDEE land surface model across US semi-arid sites. *Hydrol. Earth Syst. Sci.*, *24*(11), 5203–5230. doi: 10.5194/hess-24-5203-2020

Malek, E., & Bingham, G. E. (1993, June). Comparison of the bowen ratio-energy balance and the water balance methods for the measurement of evapotranspiration. *J. Hydrol.*, *146*, 209–220. doi: 10.1016/0022-1694(93)90276-F

McNaughton, K. G., & Van Den Hurk, B. J. J. M. (1995, May). A 'lagrangian' revision of the resistors in the two-layer model for calculating the energy budget of a plant canopy. *Bound.-Layer Meteorol.*, *74*(3), 261–288. doi: 10.1007/BF00712121

Melton, J. R., & Arora, V. K. (2016, jan). Competition between plant functional types in the Canadian Terrestrial Ecosystem Model (CTEM) v. 2.0. *Geoscientific Model Development*, *9*(1), 323–361. Retrieved from `https://doi.org/10.5194%2Fgmd-9-323-2016` doi: 10.5194/gmd-9-323-2016

Melton, J. R., Arora, V. K., Wisernig-Cojoc, E., Seiler, C., Fortier, M., Chan, E., & Teckentrup, L. (2020, jun). CLASSIC v1.0: the open-source community successor to the Canadian Land Surface Scheme (CLASS) and the Canadian Terrestrial Ecosystem Model (CTEM) – Part 1: Model framework and site-level performance. *Geoscientific Model Development*, *13*(6), 2825–2850. Retrieved from `https://doi.org/10.5194%2Fgmd-13-2825-2020` doi: 10.5194/gmd-13-2825-2020

Merlin, O., Bitar, A. A., Rivalland, V., Béziat, P., Ceschia, E., & Dedieu, G. (2011, Feb 1,). An Analytical Model of Evaporation Efficiency for Unsaturated Soil Surfaces with an Arbitrary Thickness. *Journal of Applied Meteorology and Climatology*, *50*(2), 457-471. Retrieved from `https://www.jstor.org/stable/26174034` doi: 10.1175/2010JAMC2418.1

Meyer, G., Humphreys, E. R., Melton, J. R., Cannon, A. J., & Lafleur, P. M. (2021, June). Simulating shrubs and their energy and carbon dioxide fluxes in canada's low arctic with the canadian land surface scheme including biogeochemical cycles (CLASSIC). *Biogeosciences*, *18*(11), 3263–3283. doi: 10.5194/bg-18-3263-2021

Meyer, G., Melton, J. R., & Humphreys, E. R. (2022, August). *Inclusion of a dry surface layer and modifications to the transpiration and canopy evaporation partitioning in the Canadian Land Surface Scheme Including biogeochemical Cycles (CLASSIC).* Zenodo. Retrieved from `https://doi.org/10.5281/zenodo.7015764` doi: 10.5281/zenodo.7015764

Miralles, D. G., Holmes, T. R. H., De Jeu, R. A. M., Gash, J. H., Meesters, A. G. C. A., & Dolman, A. J. (2011, February). Global land-surface evaporation estimated from satellite-based observations. *Hydrol. Earth Syst. Sci.*, *15*(2), 453–469. doi: 10.5194/hess-15-453-2011

Miralles, D. G., Jiménez, C., Jung, M., Michel, D., Ershadi, A., McCabe, M. F., ... Fernández-Prieto, D. (2016, February). The WACMOS-ET project – part 2: Evaluation of global terrestrial evaporation data sets. *Hydrol. Earth Syst. Sci.*, *20*(2), 823–842. doi: 10.5194/hess-20-823-2016

Moldrup, P., Olesen, T., Komatsu, T., Yoshikawa, S., Schjønning, P., & Rolston,

D. E. (2003, May). Modeling diffusion and reaction in soils: X. A unifying model for solute and gas diffusivity in unsaturated soil. *Soil Sci.*, *168*(5), 321. doi: 10.1097/01.ss.0000070907.55992.3c

Mu, M., De Kauwe, M. G., Ukkola, A. M., Pitman, A. J., Gimeno, T. E., Medlyn, B. E., … Ellsworth, D. S. (2021, January). Evaluating a land surface model at a water-limited site: implications for land surface contributions to droughts and heatwaves. *Hydrol. Earth Syst. Sci.*, *25*(1), 447–471. doi: 10.5194/hess-25-447-2021

Mu, Q., Heinsch, F. A., Zhao, M., & Running, S. W. (2007, December). Development of a global evapotranspiration algorithm based on MODIS and global meteorology data. *Remote Sens. Environ.*, *111*(4), 519–536. doi: 10.1016/j.rse.2007.04.015

Mu, Q., Zhao, M., & Running, S. W. (2011, August). Improvements to a MODIS global terrestrial evapotranspiration algorithm. *Remote Sens. Environ.*, *115*(8), 1781–1800. doi: 10.1016/j.rse.2011.02.019

Niu, G.-Y., Yang, Z.-L., Dickinson, R. E., Gulden, L. E., & Su, H. (2007, April). Development of a simple groundwater model for use in climate models and evaluation with gravity recovery and climate experiment data. *J. Geophys. Res.*, *112*(D7). doi: 10.1029/2006jd007522

Pastorello, G., Trotta, C., Canfora, E., Chu, H., Christianson, D., Cheah, Y.-W., … Papale, D. (2020, July). The FLUXNET2015 dataset and the ONEFlux processing pipeline for eddy covariance data. *Sci Data*, *7*(1), 225. doi: 10.1038/s41597-020-0534-3

Pinnington, E., Amezcua, J., Cooper, E., Dadson, S., Ellis, R., Peng, J., … Quaife, T. (2021, March). Improving soil moisture prediction of a high-resolution land surface model by parameterising pedotransfer functions through assimilation of SMAP satellite data. *Hydrol. Earth Syst. Sci.*, *25*(3), 1617–1641. doi: 10.5194/hess-25-1617-2021

Priestley, C. H. B., & Taylor, R. J. (1972, February). On the assessment of surface heat flux and evaporation using Large-Scale parameters. *Mon. Weather Rev.*, *100*(2), 81–92. doi: 10.1175/1520-0493(1972)100⟨0081:OTAOSH⟩2.3.CO;2

Rodríguez-Caballero, E., Chamizo, S., Roncero-Ramos, B., Román, R., & Cantón, Y. (2018, September). Runoff from biocrust: A vital resource for vegetation performance on mediterranean steppes. *Ecohydrol.*, *11*(6), e1977. doi: 10.1002/eco.1977

Savage, M. J. (2009, March). Estimation of evaporation using a dual-beam surface layer scintillometer and component energy balance measurements. *Agric. For. Meteorol.*, *149*(3), 501–517. doi: 10.1016/j.agrformet.2008.09.012

Schlesinger, W. H., & Jasechko, S. (2014, June). Transpiration in the global water cycle. *Agric. For. Meteorol.*, *189-190*, 115–117. doi: 10.1016/j.agrformet.2014.01.011

Smith, D. M., & Allen, S. J. (1996, December). Measurement of sap flow in plant stems. *J. Exp. Bot.*, *47*(12), 1833–1844. doi: 10.1093/jxb/47.12.1833

Sutanto, S. J., van den Hurk, B., Dirmeyer, P. A., Seneviratne, S. I., Röckmann, T., Trenberth, K. E., … Hoffmann, G. (2014, August). HESS opinions "a perspective on isotope versus non-isotope approaches to determine the contribution of transpiration to total evaporation". *Hydrol. Earth Syst. Sci.*, *18*(8), 2815–2827. doi: 10.5194/hess-18-2815-2014

Swart, N. C., Cole, J. N. S., Kharin, V. V., Lazare, M., Scinocca, J. F., Gillett, N. P., … Winter, B. (2019, nov). The Canadian Earth System Model version 5 (CanESM5.0.3). *Geoscientific Model Development*, *12*(11), 4823–4873. Retrieved from `https://doi.org/10.5194%2Fgmd-12-4823-2019` doi: 10.5194/gmd-12-4823-2019

Swenson, S. C., & Lawrence, D. M. (2014, Sep 16,). Assessing a dry surface layer-based soil resistance parameterization for the Community Land Model using

GRACE and FLUXNET-MTE data. *Journal of Geophysical Research: Atmospheres*, *119*(17), 10,299-10,312. doi: 10.1002/2014JD022314

Véliz-Chávez, C., Mastachi-Loza, C. A., González-Sosa, E., Becerril-Piña, R., & Ramos-Salinas, N. M. (2014). Canopy storage implications on interception loss modeling. *Am. J. Plant Sci.*, *05*(20), 3032–3048. doi: 10.4236/ajps.2014.520320

Vereecken, H., Weihermüller, L., Assouline, S., Šimůnek, J., Verhoef, A., Herbst, M., ... Xue, Y. (2019, January). Infiltration from the pedon to global grid scales: An overview and outlook for land surface modeling. *Vadose Zone J.*, *18*(1), 1–53. doi: 10.2136/vzj2018.10.0191

Verseghy, D. (2017). *CLASS-The Canadian Land Surface Scheme (v.3.6.2)* (Tech. Rep.). Climate Research Divison, Science and Technology Branch, Environment and Climate Change Canada.

Wang, A., Price, D. T., & Arora, V. (2006, September). Estimating changes in global vegetation cover (1850-2100) for use in climate models. *Global Biogeochem. Cycles*, *20*(3). doi: 10.1029/2005GB002514

Wang, K., & Dickinson, R. E. (2012, June). A review of global terrestrial evapotranspiration: Observation, modeling, climatology, and climatic variability. *Rev. Geophys.*, *50*(2). doi: 10.1029/2011rg000373

Wang, L., Good, S. P., & Caylor, K. K. (2014, October). Global synthesis of vegetation control on evapotranspiration partitioning. *Geophys. Res. Lett.*, *41*(19), 6753–6757. doi: 10.1002/2014gl061439

Wang, P., Niu, G.-Y., Fang, Y.-H., Wu, R.-J., Yu, J.-J., Yuan, G.-F., ... Scott, R. L. (2018, March). Implementing dynamic root optimization in Noah-MP for simulating phreatophytic root water uptake. *Water Resour. Res.*, *54*(3), 1560–1575. doi: 10.1002/2017wr021061

Warren, R. K., Pappas, C., Helbig, M., Chasmer, L. E., Berg, A. A., Baltzer, J. L., ... Sonnentag, O. (2018, July). Minor contribution of overstorey transpiration to landscape evapotranspiration in boreal permafrost peatlands: Contribution of overstory transpiration in a boreal permafrost peatland. *Ecohydrol.*, *11*(5), e1975. doi: 10.1002/eco.1975

Wei, Z., Yoshimura, K., Wang, L., Miralles, D. G., Jasechko, S., & Lee, X. (2017, March). Revisiting the contribution of transpiration to global terrestrial evapotranspiration: Revisiting global ET partitioning. *Geophys. Res. Lett.*, *44*(6), 2792–2801. doi: 10.1002/2016GL072235

Zhang, L., Jiang, H., Wei, X., Zhu, Q., Liu, S., Sun, P., & Liu, J. (2008, October). Evapotranspiration in the meso-scale forested watersheds in minjiang valley, west china1. *J. Am. Water Resour. Assoc.*, *44*(5), 1154–1163. doi: 10.1111/j.1752-1688.2008.00245.x

Zhang, Y., Peña-Arancibia, J. L., McVicar, T. R., Chiew, F. H. S., Vaze, J., Liu, C., ... Pan, M. (2016, January). Multi-decadal trends in global terrestrial evapotranspiration and its components. *Sci. Rep.*, *6*, 19124. doi: 10.1038/srep19124